

 Open access • Posted Content • DOI:10.1101/2020.12.01.404483

Topoisomerase 1 inhibition therapy protects against SARS-CoV-2-induced inflammation and death in animal models. — [Source link](#)

[Jessica Sook Yuin Ho](#), [Bobo Wing-Yee Mok](#), [Laura Campisi](#), [Tristan X. Jordan](#) ...+43 more authors

Institutions: [Icahn School of Medicine at Mount Sinai](#), [University of Hong Kong](#), [Kansas State University](#), [Columbia University](#) ...+5 more institutions

Published on: 01 Dec 2020 - [bioRxiv](#) (Cold Spring Harbor Laboratory)

Topics: [Proinflammatory cytokine](#)

Related papers:

- [Cancer vs. SARS-CoV-2 induced inflammation, overlapping functions, and pharmacological targeting.](#)
- [Overactive Epidermal Growth Factor Receptor Signaling Leads to Increased Fibrosis after Severe Acute Respiratory Syndrome Coronavirus Infection.](#)
- [The pro-inflammatory cytokines in COVID-19 pathogenesis: What goes wrong?](#)
- [Impact of cytokine storm and systemic inflammation on liver impairment patients infected by SARS-CoV-2: Prospective therapeutic challenges.](#)
- [Treating exuberant, non-resolving inflammation in the lung; implications for acute respiratory distress syndrome and COVID-19](#)

Share this paper:    

View more about this paper here: <https://typeset.io/papers/topoisomerase-1-inhibition-therapy-protects-against-sars-cov-1wnty3s8ke>

1 Topoisomerase 1 inhibition therapy protects against SARS-CoV-2- 2 induced inflammation and death in animal models.

3
4 Jessica Sook Yui Ho^{1,*}, Bobo Wing-Yee Mok^{2,*}, Laura Campisi¹, Tristan Jordan¹,
5 Soner Yildiz¹, Sreeja Parameswaran⁴, Joseph A Wayman^{9,27}, Natasha N Gaudreault¹⁰, David
6 A Meekins¹⁰, Sabarish V. Indran¹⁰, Igor Morozov¹⁰, Jessie D Trujillo¹⁰, Yesai S Fstchyan¹,
7 Raveen Rathnasinghe¹, Zeyu Zhu¹, Simin Zheng¹, Nan Zhao¹, Kris White¹, Helen Ray-Jones³,
8 Valeriya Malysheva³, Michiel J Thiecke²⁶, Siu-Ying Lau², Honglian Liu², Anna Junxia Zhang²,
9 Andrew Chak-Yiu Lee², Wen-Chun Liu¹, Teresa Aydillo¹, Betsaida Salom Melo^{12,13}, Ernesto
10 Guccione¹¹, Robert Sebra^{12,13,29,30}, Elaine Shum⁵, Jan Bakker^{14,15,16}, David A. Kaufman¹⁷, Andre
11 L. Moreira¹⁸, Mariano Carossino¹⁹, Udeni B R Balasuriya¹⁹, Minji Byun²⁰, Emily R Miraldi^{9,27},
12 Randy A Albrecht^{1,21}, Michael Schotsaert^{1,21}, Adolfo Garcia-Sastre^{1, 21,22}, Sumit K Chanda²³,
13 Anand D Jeyasekharan⁶, Benjamin R TenOever^{1,21,24}, Mikhail Spivakov³, Matthew T
14 Weirauch^{4,25, 28}, Sven Heinz⁷, Honglin Chen², Christopher Benner⁷, Juergen A Richt^{8,10}, Ivan
15 Marazzi^{1,21}.

16
17 ¹Department of Microbiology, Icahn School of Medicine at Mount Sinai, New York, NY 10029, USA.

18 ²Department of Microbiology and State Key Laboratory for Emerging Infectious Diseases, The University of Hong Kong, L-501, Li Ka
19 Shing

20 ³MRC London Institute of Medical Sciences, London W12 0NN, UK

21 ⁴Center for Autoimmune Genomics and Etiology, Cincinnati Children's Hospital Medical Center, Cincinnati, OH 45229, USA;

22 ⁵Division of Medical Oncology and Hematology, NYU Langone Perlmutter Cancer Center, New York, NY 10016, USA.

23 ⁶Department of Haematology-Oncology, National University Hospital and Cancer Science Institute of Singapore, National University
24 of Singapore, 117599 Singapore.

25 ⁷Department of Medicine, School of Medicine, University of California San Diego, La Jolla, CA 92092, USA

26 ⁸Center of Excellence for Emerging and Zoonotic Animal Diseases (CEEZAD), Kansas State University, Manhattan, KS

27 ⁹Divisions of Immunobiology and Biomedical Informatics, Cincinnati Children's Hospital, Cincinnati, OH 45229, USA;

28 ¹⁰Diagnostic Medicine and Pathobiology, College of Veterinary Medicine, Kansas State University, 1800 Denison Avenue,
29 Manhattan, KS, 66506, USA

30 ¹¹Tisch Cancer Institute, Department of Oncological Sciences and Department of Pharmacological Sciences, Icahn School of
31 Medicine at Mount Sinai, New York City, NY, USA

32 ¹²Department of Genetics and Genomics, Icahn School of Medicine at Mount Sinai, New York, NY, USA.

33 ¹³Icahn Institute of Genomics and Multiscale Biology, Icahn School of Medicine at Mount Sinai, New York, NY, USA.

34 ¹⁴Pontificia Universidad Católica de Chile, Santiago, Chile

35 ¹⁵Erasmus MC University Medical Center Rotterdam, Rotterdam, The Netherlands.

36 ¹⁶Editor in Chief, Journal of Critical Care, NYU School of Medicine, Columbia University College of Physicians & Surgeons, New
37 York, USA.

38 ¹⁷Division of Pulmonary, Critical Care, and Sleep Medicine, Department of Medicine, NYU School of Medicine

39 ¹⁸Department of Pathology, New York University School of Medicine

40 ¹⁹Louisiana Animal Disease Diagnostic Laboratory and Department of Pathobiological Sciences, School of Veterinary Medicine,
41 Louisiana State University, Baton Rouge, LA, USA

42 ²⁰Department of Medicine, Clinical Immunology, Icahn School of Medicine at Mount Sinai, New York, NY, USA.

43 ²¹Global Health and Emerging Pathogens Institute, Icahn School of Medicine at Mount Sinai, New York, NY, USA.

44 ²²Department of Medicine, Division of Infectious Diseases, Icahn School of Medicine at Mount Sinai, One Gustave L. Levy Place,
45 Box 1124, New York, NY 10029, USA.

46 ²³Immunity and Pathogenesis Program, Infectious and Inflammatory Disease Center, Sanford Burnham Prebys Medical Discovery
47 Institute, La Jolla, CA 92037.

48 ²⁴Virus Engineering Center for Therapeutics and Research, Icahn School of Medicine at Mount Sinai, New York, NY, USA

49 ²⁵Department of Pediatrics, University of Cincinnati, College of Medicine, Cincinnati, OH, 45229, USA.

50 ²⁶Enhanc3D Genomics Ltd, Cambridge CB22 0AT

51 ²⁷Department of Pediatrics, University of Cincinnati, College of Medicine, Cincinnati, OH, 45229, USA.

52 ²⁸Divisions of Biomedical Informatics and Developmental Biology, Cincinnati Children's Hospital Medical Center, Cincinnati, OH
53 45229, USA.

54 ²⁹Sema4, a Mount Sinai venture, Stamford CT, USA

55 ³⁰Black Family Stem Cell Institute, Icahn School of Medicine at Mount Sinai, NY, NY 10029

56 * These authors contributed equally

57

58 **SUMMARY**

59
60 The ongoing pandemic caused by Severe Acute Respiratory Syndrome Coronavirus 2 (SARS-
61 CoV-2) is currently affecting millions of lives worldwide. Large retrospective studies indicate that
62 an elevated level of inflammatory cytokines and pro-inflammatory factors are associated with
63 both increased disease severity and mortality. Here, using multidimensional epigenetic,
64 transcriptional, *in vitro* and *in vivo* analyses, we report that Topoisomerase 1 (Top1) inhibition
65 suppresses lethal inflammation induced by SARS-CoV-2. Therapeutic treatment with two doses
66 of Topotecan (TPT), a FDA-approved Top1 inhibitor, suppresses infection-induced inflammation
67 in hamsters. TPT treatment as late as four days post-infection reduces morbidity and rescues
68 mortality in a transgenic mouse model. These results support the potential of Top1 inhibition as
69 an effective host-directed therapy against severe SARS-CoV-2 infection. TPT and its derivatives
70 are inexpensive clinical-grade inhibitors available in most countries. Clinical trials are needed to
71 evaluate the efficacy of repurposing Top1 inhibitors for COVID-19 in humans.

72
73 **INTRODUCTION**

74 Coronavirus disease 2019 (COVID-19) is an infectious disease caused by severe acute
75 respiratory syndrome coronavirus 2 (SARS-CoV-2).

76
77 As of 16 November 2020, 54 million people have been infected and 1.33 million have died
78 [<https://coronavirus.jhu.edu/map.html>, accessed 16 Nov 2020]. It is currently estimated that
79 approximately 40-45% of SARS-CoV-2 infections are asymptomatic (Oran and Topol, 2020).
80 For the remaining patients with symptomatic infections, data from China, Italy and the United
81 States indicate that approximately 80% of infections are mild (not requiring hospitalization), 15%
82 are moderate to severe (requiring hospitalization), and 5% are critical (requiring intensive care
83 unit (ICU) care)(Garg et al., 2020; Livingston and Bucher, 2020; Stokes et al., 2020; Wu and
84 McGoogan, 2020).

85
86 The most common manifestation of severe COVID-19 is acute hypoxemic respiratory failure,
87 often associated with shock or multi-organ failure (Bhatraju et al., 2020; Wang et al., 2020a; Wu
88 et al., 2020). Shock and multiorgan failure may be related to complications of critical illness; For
89 example, ventilator-associated lung injury (Slutsky and Ranieri, 2013), secondary infection
90 (Yang et al., 2020a) and aggravation of underlying chronic organ dysfunction(Cummings et al.,
91 2020) .

92
93 In most countries, the infection fatality rate is around 0.5-1%, and exponentially increases to up
94 to 10% when referencing more susceptible age groups and people with pre-existing
95 conditions(O'Driscoll et al., 2020). Therefore, the development of effective treatment plans for
96 severe COVID-19 is imperative.

97
98 SARS-CoV-2 displays similar pathogenic mechanisms to that of SARS-CoV-1
99 (Channappanavar and Perlman, 2017; Zhu et al., 2020). The main hallmarks of disease
100 progression feature two phases: a first phase of increasing viremia, followed by a subsequent
101 steep increase in systemic inflammation (Lee et al., 2020; Merad and Martin, 2020; Siddiqi and
102 Mehra, 2020). In fact, SARS-CoV-1 and SARS-Cov-2 patients who require intensive care
103 showed elevated plasma levels of inflammatory cytokines and chemo-attractants (Chen et al.,
104 2020; Del Valle et al., 2020; Huang et al., 2020; Lucas et al., 2020; Qin et al., 2020; Wang et al.,
105 2020b; Yang et al., 2020b; Zhou et al., 2020a)

106
107 Several studies have shown that levels of inflammatory molecules can help distinguish those
108 that survive COVID-19 from those that do not. For example, increased levels of IL-6, fibrin

109 degradation products (D-dimer), as well as other single measurements like CRP or combined-
110 measurement parameters (SOFA score) have been correlated with risk for death from COVID-
111 19. (Zhou et al., 2020a). Notably, all non-survivors experienced sepsis (Zhou et al., 2020a).
112 Therefore, increased systemic inflammation, occurring during disease progression, provides a
113 biological rationale for interrupting hyper-inflammation to reduce disease severity. Guided by
114 this logic, clinical trials have begun to examine the efficacy of cytokine blockers and anti-
115 inflammatory molecules as potential COVID-19 therapeutics (Merad and Martin, 2020).

116
117 However, inhibition of single cytokines such as IL-6 or GM-CSF might not be sufficient (Hermine
118 et al., 2020; Salvarani et al., 2020). This is due to the fact that many signaling molecules and
119 pathways are involved in triggering an inflammatory response. Additionally, levels of individual
120 cytokines can vary depending on the age and the clinical history of the patient, thus limiting the
121 scope of therapeutics that only target a single inflammatory molecule.

122
123 A rapid induction of gene expression serves as a fundamental mechanism in activating an
124 inflammation response. Inhibition of this process might hold the key to the development of novel
125 therapeutics for COVID-19. Previously, we have reported that chromatin factors play key roles
126 in controlling the induction of inflammatory gene expression programs (Marazzi et al., 2012;
127 Miller et al., 2015; Nicodeme et al., 2010). Targeting the activity of these proteins acting on the
128 chromatin template, where infection-induced gene transcription is executed, leads to the
129 concerted suppression of multiple antiviral and anti-inflammatory genes (Marazzi et al., 2012;
130 Miller et al., 2015; Nicodeme et al., 2010). Such simultaneous inhibition of many virus-induced
131 genes “in one go” can have a clear advantage over conventional single target therapies
132 (Marazzi et al., 2018). In particular, we have previously shown that the host enzyme
133 topoisomerase 1 (Top-1) is required to selectively activate the expression of inflammatory genes
134 during viral and bacterial infection and co-infections (Rialdi et al., 2016). Therapeutic
135 administration (after infection) of one to three doses of topoisomerase inhibitors can rescue
136 mortality in four animal models of inflammation-induced death (Rialdi et al., 2016). These data
137 support the hypothesis that host-directed epigenetic therapy can be valuable to suppress hyper-
138 inflammatory responses in the context of infectious diseases. We present here, a series of
139 experiments in which we tested the hypothesis that epigenetic therapy aimed at modifying the
140 host response to SARS-CoV-2 infection would ameliorate severe COVID-19.

141 142 **RESULTS**

143
144 Cell signaling cascades converge on chromatin to dictate changes in gene expression programs
145 upon cell intrinsic and extrinsic signals. We performed a combined structural and epigenetic
146 analysis during infection in an effort to understand how SARS-CoV-2 alters chromatin function
147 and the epigenetic landscape of cells upon infection,

148
149 To characterize structural chromatin changes we performed Hi-C, a technique that profiles the
150 three-dimensional architecture of the genome (Bonev and Cavalli, 2016; Hildebrand and
151 Dekker, 2020). Hi-C was performed on uninfected and SARS-CoV-2 infected A549 cells
152 expressing the human SARS-CoV-2 entry receptor Ace2 (A549-ACE2) at both early (8 hours)
153 and late (24 hours) time points post infection, in order to investigate the dynamics of infection
154 induced changes on chromatin structure. Reproducible results were achieved across replicates
155 for all time points. (**Table S1**). Our analysis indicates that large portions of the genome alter
156 their global interaction profiles as infection progresses, culminating in a major redistribution of
157 chromatin associated with either the active (A) or inactive (B) compartments at the 24h time
158 point (**Figure 1A**). Notably, compartment changes result in a shortening of the domain size, with
159 large linear stretches of A and B compartment chromatin generally becoming subdivided into

160 smaller A/B domains (**Figure 1A and 1B**), a feature that partially phenocopies the loss of
161 regional topological constraints controlled by cohesin (Rao et al., 2017; Schwarzer et al., 2017).

162
163 To characterize whether the structural changes seen using Hi-C were associated with
164 epigenetic features of gene activation and repression, we performed ChIP-sequencing for
165 H3K27 acetylation (K27ac), an epigenetic mark found at active regulatory regions that is
166 commonly used to monitor dynamic changes in transcriptional activation. ChIP-seq for H3K27ac
167 was performed in uninfected and infected A549-ACE2 cells at the same time points as the Hi-C.
168 Our analysis showed high correlation of K27ac levels between replicates (**Figure S1A**). While
169 some regions of the genome showed no change in K27ac levels upon infection (cluster i; **Figure**
170 **S1B and S1C**), there were statistically significant changes in K27ac levels at promoters and
171 other regulatory regions during the course of infection (clusters ii to vii; **Figure S1B and S1C**;
172 **Table S2A-S2C**). Regions that significantly gain (clusters v and vi; **Figure S1B**) and lose K27ac
173 (clusters ii and iii; **Figure S1B**) over the course of infection were detected.

174
175 We labelled changes in K27ac across condition as “K27 loss” to describe instances in which
176 reduction of K27ac signal across the genome occurs during infection compared to the
177 uninfected condition. Increased genomic level of K27ac during infection was labelled as “K27
178 gain”.

179
180 Overlaying the changes in K27ac with structural chromatin changes indicate that regions
181 gaining or losing K27ac are enriched in chromatin domains that move from B-A or A-B
182 compartment, respectively (**Figure 1C**). This partitioning occurs dynamically throughout the
183 infection (**Figure 1C** -compare 8h vs 24h) and is associated with gene expression activity
184 (**Figure 1D**). These results suggest that the dynamic restructuring of genome
185 compartmentalization by SARS-CoV-2 infection is highly associated with transcriptional activity.

186
187 To characterize whether a unique set of transcription factors might participate in partitioning
188 chromatin into active or inactive regions during infection, we performed DNA binding site motif
189 enrichment analysis of regions displaying differential H3K27ac activity. Our results indicate that
190 repressed regions lack unique enrichment of immune-specific transcription factors at promoters,
191 enhancers, and other putative regulatory regions (**Figure S1D, Table S3**). Regions that gain
192 K27ac signal are largely devoid of unique transcription factor signatures apart from a strong
193 enrichment for motifs recognized by NF- κ B (red bars, cluster v and vi; **Figure S1D, Table S3**), a
194 master regulator of inflammatory gene programs.

195
196 Overall, our results indicate that SARS-CoV-2 induces global epigenetic and structural changes
197 in the infected cell, underlying the identity of inducible regulatory networks controlling cell
198 responses to infection.

199 200 **Topoisomerase I controls SARS-CoV-2-induced gene expression response**

201 To determine whether chromatin factors can control the induction of the cell response by
202 promoting the transactivation of SARS-CoV-2-induced gene program, we focused our attention
203 on topoisomerase I (Top1), a factor known to activate bacterial- and viral infection- induced
204 genes (Rialdi et al., 2016). We performed siRNA-mediated knockdown of Top1 (siTOP1) along
205 with control siRNA (siSCR) in A549-ACE2 cells, followed by mock treatment (PBS only;
206 uninfected controls) or infection with SARS-CoV-2. Gene expression changes in these cells
207 were quantified by RNA-sequencing at 24 hours post infection. Our analyses indicate that
208 siTOP1 treated cells had a distinct transcriptional response to the virus (**Figure 2A**) as
209 compared to no siRNA or siSCR treated cells, and that depletion of Top1 resulted in selective
210 suppression of many infection-induced genes (Fold Change > 1.5, padj<0.05; **Figure 2B and**

211 **2C, Table S4**). Gene ontology pathway analyses of genes that are downregulated upon Top1
212 knockdown suggest that many of these genes are involved in inflammatory responses (**Figure**
213 **2C, Table S5**). We further validated our results by qPCR for representative genes IL-6, CXCL8
214 and TOP1 (**Figure 2D**), verifying that depletion of Top1 reduces the expression of these
215 inflammatory genes.

216
217 To understand the specificity of Top1, we profiled infection induced and Top1 dependent genes
218 (“Dep.”; **Table S4C**) identified in Figure 2B with respect to their structural and epigenetic status
219 at basal state and after infection. As controls, we used all expressed genes (“Exp”; **Table S4C**)
220 or genes that are also induced by infection but unaffected by Top1 depletion (Top1
221 independent, “Indep.”; **Table S4C**). Our analysis indicates that genes that depend on Top1 for
222 their upregulation are induced to higher levels than Top1 independent genes upon infection
223 (**Figure 2E**). Top1 dependent genes also displayed greater shifts towards active chromatin
224 compartment (positive delta PC1 levels, **Figure 2F**) and increases in K27ac signals (positive
225 delta H3K27ac levels; **Figure 2G**) compared to Top1 independent genes. Differences were
226 more pronounced later in infection (**Figures 2F and 2G**).

227
228 Overall our analysis indicates that Top1-dependent genes are highly inducible during SARS-
229 CoV-2 infection as a result of chromatin and epigenetic changes that render their transactivation
230 permissible.

231
232 **Top1 inhibition suppresses lung inflammation and lung damage in infected hamsters.**

233
234 To determine whether inhibition of Top1 activity can dampen inflammatory gene expression *in*
235 *vivo*, we selected topotecan (TPT), a FDA approved Top1 inhibitor, to use in the Syrian Golden
236 hamster model (Munoz-Fontela et al., 2020) (hereafter referred as hamster) of SARS-CoV-2
237 infection.

238
239 We treated SARS-CoV-2 infected hamsters with either vehicle control (DMSO) or 10mg/kg TPT
240 at days 1 and 2 post-infection. Lungs from these animals were then collected for histology and
241 transcriptome analysis at days 4 and 6 post-infection (**Figure 3A**).

242
243 Clustering of RNA-seq reads using principal component analysis (PCA) indicates that the gene
244 expression profiles under the three conditions (uninfected, infected-DMSO treated, and infected-
245 TPT treated) partition based on infection, treatment status, and the temporality of the infection
246 (day 4 and 6), with each replicate clustering in close proximity to its counterpart (**Figure 3B**).

247
248 Differential expression (DE) analysis showed that TPT suppresses inflammatory gene
249 expression in the lungs of infected hamsters (**Figure 3C and 3D**). Clustering of the DE data
250 indicates that the gene expression profiles of TPT-treated infected lungs are more similar to that
251 of the non-infected lungs, rather than infected ones (**Figure 3C**). The GO categories associated
252 with the TPT-suppressed genes indicates specific inhibition of virus-induced and inflammatory
253 genes at both day 4 and day 6 post-infection (**Figure 3D**).

254
255 Histopathological analysis of infected, DMSO vehicle-treated hamster lungs at days 4 and 6
256 post-infection displayed diffused alveoli destruction, bronchiolar epithelium cell death and
257 hemorrhaging, coupled with massive immune cell infiltration and exudation, typically associated
258 with increased expression of inflammatory mediators and recruitment of immune cells during
259 infection (**Figure 3E and 3F**). On the contrary, TPT treatment diminished pathological features
260 of lung damage in infected animals. Lungs from these animals did not have conspicuous

261 alveolar space infiltration, exudation or hemorrhaging at both days 4 and 6 post infection
262 (**Figure 3G and 3H**).

263 To determine the clinical significance of our observations, we then asked if the genes that were
264 downregulated by TPT treatment in SARS-CoV-2 infected hamsters also corresponded to
265 immunopathological gene signatures that have been observed in COVID-19 patients. Cross-
266 comparison of our results with the gene expression profiles in human lungs isolated from
267 autopsies of COVID-19 patients and uninfected control lungs (Nienhold et al., 2020) indicated
268 that TPT suppressed genes that are hyperactivated in patients who succumbed to infection
269 (**Figure 4A and 4B**). In fact, TPT-inhibited genes are up-regulated in COVID-19 lung autopsy
270 tissue relative to healthy control ($P < 1E-3$) (**Figure 4A, left panel**), while genes up-regulated by
271 TPT are down-regulated in COVID-19 lung relative to control ($P < 1E-7$) (**Figure 4A, right**
272 **panel**). These results suggest that treatment with TPT might reverse COVID-19-induced lung
273 gene expression responses. The gene expression profiles of TPT inhibited genes in individual
274 patients (**heatmap, Figure 4B**) and the corresponding gene set enrichment scores are shown in
275 **Figure 4B**.

276 We next sought to validate whether lower dosages of TPT, which are associated with negligible
277 cytostatic effects (Guichard et al., 2001; Houghton et al., 1995; Nemati et al., 2010), were
278 effective in suppressing SARS-CoV-2 infection induced inflammation. We performed a parallel
279 experiment to the one described in **Figure 4A** using 5-fold lower TPT (2mg/kg) and the same
280 regimen of TPT treatment at Day 1 and 2 post-infection (**Figure S2A**). Lungs from infected and
281 treated hamsters were assayed at Day 4 post infection.

282
283 Animals treated with TPT had reduced lung to body weight ratios post infection (**Figure S2B**),
284 which suggest reduced pulmonary edemas in these animals. In line with this, histopathological
285 analyses showed reduced broncho-pneumonia (**Figure S2C-S2E**) and immune cell infiltration
286 (**Table S6**) in the lungs of TPT treated animals when compared to DMSO treated ones. qPCR
287 analysis of representative genes also suggested reduced expression of inflammatory genes in
288 TPT treated animals (**Figure S2F**). Overall, these results suggest that lower doses of TPT
289 treatment can still effectively suppress the expression of inflammatory molecules, and
290 ameliorate inflammation induced pathology during SARS-CoV-2 infection.

291
292 In sum, our results support the hypothesis that TPT suppresses SARS-CoV-2-induced lung
293 inflammation in vivo.

294
295 **Top1 inhibition therapy suppresses, SARS-CoV-2 morbidity and lethality in transgenic**
296 **mice.**

297
298 To further verify our results, we extended our studies to a complementary model and evaluated
299 the effects of TPT treatment in transgenic mice that express the human angiotensin I-converting
300 enzyme 2 (ACE2) receptor under the cytokeratin 18 gene promoter (K18-hACE2). This mouse
301 strain is susceptible to SARS-CoV-2 infection and displays a disease progression profile that
302 shares many features of severe COVID-19 (Winkler et al., 2020). Importantly, loss of pulmonary
303 function and weight loss in these mice occurs after the peak of viral replication, and coincides
304 with infiltration of immune cells (monocytes, T cells, neutrophils) in the lung and alveolar
305 spaces at day 4 post infection (Winkler et al., 2020). As such, K18-hACE2 have been suggested
306 as a model to define the basis of SARS-CoV-2-induced lung disease and test immune and
307 antiviral countermeasures (Bao et al., 2020; Winkler et al., 2020).

308
309 To test whether inhibition of inflammation provides a protective effect in infected K18-hACE2
310 mice, we performed three different regimes of TPT treatments, labelled as early, intermediate,
311 and late, to respectively describe dosing of the inhibitor at 2mg/kg on days 1+2, days 3+4; or
312 days 4+5 post-infection respectively (**Figure 5A**).

313
314 The rationale behind this approach is that inhibition of inflammation could be detrimental during
315 the early phases of the infection, as it might cause increased viral replication and dissemination.
316 The optimal protective effect of inhibiting inflammation should be achieved during the hyper-
317 inflammatory phase of the disease, which would coincide with the later stage of infection.

318
319 Indeed, our results showed that early treatment of TPT is ineffective in reducing the morbidity
320 and mortality caused by SARS-2 infection (**Figure 5B and 5C: TPT: D1+D2**). Intermediate
321 treatment ameliorates morbidity but not mortality (**Figure 5B and 5C: TPT: D3+D4**). Strikingly,
322 late TPT treatment suppresses both morbidity and mortality (**Figure 5B and 5C: TPT: D4+D5**).
323 TPT treatment is associated with suppression of inflammatory gene expression in the lung, as
324 indicated by qPCR of representative genes IL-6, CXCL3 and CCR8 (**Figure 5D**).

325
326 Our results indicate that inhibition of hyper-inflammation by therapeutic administration of TPT
327 can rescue K18-hACE2 mice from lethal SARS-CoV-2 infection.

328 329 **DISCUSSION**

330
331 The ongoing COVID-19 pandemic caused by SARS-CoV-2 is currently affecting millions of lives
332 worldwide, and poses an overwhelming burden on global health systems as well as the
333 economy. The development of novel therapeutics against SARS-CoV-2 remains a top priority.
334 While prophylactic measures are being evaluated and distributed, drugs available to target
335 SARS-CoV-2 and function therapeutically are direly needed especially for severe cases of
336 COVID-19.

337
338 Although the pathophysiology of SARS-CoV-2 has not yet been fully characterized, it has been
339 observed that SARS-CoV-2 infection triggers hyper- activation of pro-inflammatory cytokines
340 (IL-6, -Il1b, TNFa) and chemokines (CXCL8, 9, 10, CCL2) (Huang et al., 2020; Lucas et al.,
341 2020; Merad and Martin, 2020; Tang et al., 2020; Zhou et al., 2020a). The increased level of
342 inflammatory molecules has been shown to correlate with COVID-19 disease severity (Del Valle
343 et al., 2020; Moore and June, 2020). While the exact mechanism and cell type-specific
344 contributions to hyper-inflammation still needs to be fully elucidated, monocytes, macrophages
345 and dendritic cells are primary candidates and have been reported to contribute to the cytokine-
346 mediated immunopathology seen in human (Del Valle et al., 2020; Giamarellos-Bourboulis et
347 al., 2020; Moore and June, 2020). This is supported by previous studies of the immune
348 response against SARS-CoV-1 and MERS-CoV infections (Cheung et al., 2005; Wong et al.,
349 2004). Additionally, non-myeloid cells have been recently shown to contribute to the hyper-
350 inflammatory program (Zhou et al., 2020b). Elevated inflammatory response contributes to
351 sepsis and multi-organ failure, an important contributor to death from COVID-19 (Zhou et al.,
352 2020a). Therefore, treatments that can suppress host inflammatory response might be
353 potentially effective therapeutic strategies for COVID-19. In this light, it is important to highlight
354 that glucocorticosteroids (dexamethasone, methylprednisolone, hydrocortisone), which act as
355 suppressors of systemic inflammation, have been reported to ameliorate the outcome of
356 COVID-19, especially in hospitalized patients who require supplemental oxygen (Group et al.,
357 2020).

358

359 **Structural and functional changes in the genome upon infection**

360
361 While our knowledge of SARS-CoV-2 pathogenesis is expanding rapidly, little is known about
362 how epigenetic modifications and genome structure are affected by infection, and in what
363 capacity they affect gene activity (Liu et al., 2020). Our data suggest that SARS-CoV-2 infection
364 imposes a pervasive effect on the host cell response at the genome organization level, causing
365 drastic changes in both the segmentation and interaction patterns of chromatin regions. The
366 SARS-CoV-2 infection-induced chromatin segregation pattern mirrors what observed in cells
367 depleted of cohesin, a protein that maintains chromosomal architecture (Hnisz et al., 2016;
368 Schwarzer et al., 2017). In both SARS-CoV-2 infection and absence of cohesin, large stretches
369 of A and B compartments become subdivided into smaller A/B domains, leading to reduction in
370 compartment domain size. These effects are likely indicative of increased chromatin fiber
371 flexibility, allowing it to segregate more easily according to the activity of the embedded
372 regulatory elements. Future work is needed to understand the implications of this events for
373 infection response.

374
375 Regarding SARS-CoV-2 infection-induced compartment movement, we surmise that A-to-B and
376 B-to-A switches are driven by transcriptional and epigenome activity. While A-B transitions are
377 characterized by decreased K27ac at promoters and gene suppression, B-A is accompanied by
378 increased K27ac at promoters and gene induction. Gene suppression has functional
379 consequences as it affects many conventional infection-induced genes activated by STAT1/2
380 and IRF3 transcription factors. Suppression is likely a result of viral antagonism. In fact, a
381 recent report elucidates the pleiotropy of viral antagonism mechanisms and their collective
382 effects on suppressing host functions at transcriptional, co-transcriptional and post-
383 transcriptional levels (Banerjee et al., 2020; Lei et al., 2020). Gene activation is the result of
384 signal-induced transactivation, and indicates that many cellular genes escape viral suppression
385 during infection. One prominent example is a subset of inflammatory genes whose expression is
386 driven by infection-activated transcription factor NF- κ B. The proteins encoded by these genes
387 are potent pro-inflammatory molecules and present systemically with high levels in severe
388 COVID-19 patients (Del Valle et al., 2020; Moore and June, 2020). The selective and concerted
389 induction of inflammatory genes provides the rationale for using epigenetic inhibitors to
390 suppress their induction and establish a global anti-inflammatory state (Marazzi et al., 2018).

391 **Top1 inhibition therapy**

392
393
394 We show that the host enzyme Topoisomerase-1 promotes transcriptional activation of pro-
395 inflammatory genes during SARS-CoV-2 infection. We then demonstrate that Top1 inhibition
396 limits the expression of inflammatory genes in the lungs of infected animals. Most importantly,
397 Top1 inhibition decreases morbidity and morbidity in infected mice. The therapeutic effect can
398 be achieved by drug administration 4-5 days following infection.

399
400 Whether the suppression of inflammation *in vivo* is solely the result of dampened epithelial
401 response, or whether it affects, directly or indirectly neutrophil/monocytic activation or immune
402 cell recruitment to the lung remains unknown. We posit that TPT action in both epithelial and
403 immune cells responses result in the positive outcomes, as TPT is likely to suppress inducible
404 transcriptional programs in both the infected cells and by-stander cells. Dampening highly
405 inducible genes and sparing housekeeper genes is a typical feature of epigenetic inhibitors that
406 act on signal-induced genes, which aside from the requirement of cofactors for their activation
407 have unifying genomic features like high burst rates conferred by many regulatory
408 enhancers(Chen et al., 2019; Fukaya et al., 2016; Marazzi et al., 2018; Senecal et al., 2014;
409 Zabidi et al., 2015).

410
411 In sum, TPT and other Top1 inhibitors like irinotecan are widely available and FDA-approved.
412 Some are in the WHO list of Essential Medicines. They are inexpensive and generic formulation
413 exists throughout the world, making them easily accessible for immediate use. Overall, our
414 results suggest that repurposing of TOP1 inhibitor could be a valuable strategy to ameliorate or
415 treat severe COVID-19.

416 417 **Pharmacokinetics considerations and limitations of this study**

418 Although the preclinical animal models of SARS-CoV-2 pathogenesis used here are, as with
419 any animal model, only partially representative of the biology of humans, our study indicates a
420 promising effect of TPT by suppressing inflammation in COVID-19. Several factors require
421 careful consideration prior to extrapolating these results towards the design of clinical trials of
422 Top1-inhibition therapy for human COVID-19. First, in our animal models, we can suppress
423 inflammation and reduce disease pathology in the lung using 2 doses of Top1 inhibition therapy
424 with TPT at 2mg/kg intraperitoneally. This equates to a 5-fold reduction from typical
425 chemotherapeutic anti-cancer doses in rodent models (Guichard et al., 2001; Houghton et al.,
426 1995; Nemati et al., 2010). In clinical practice, the Top1 inhibitors TPT and Irinotecan have well-
427 characterized pharmacokinetics and toxicity profiles (Kollmannsberger et al., 1999; Mathijssen
428 et al., 2001), albeit in patients without SARS-CoV-2 infection. Doses that are 5-fold lower than
429 those used in the treatment of small-cell lung cancer (TPT)(Rowinsky et al., 1992; von Pawel et
430 al., 1999) and colorectal cancer (irinotecan)(Andre et al., 1999) are expected to cause little to no
431 toxicity, and importantly no risk of neutropenia. This significant dose reduction, together with the
432 wealth of clinical experience in the use of TPT and irinotecan should reassure us about potential
433 concerns over cytotoxicity. Nonetheless, safety trials of the reduced dosage of TPT or irinotecan
434 in COVID-19 patients will need to be performed prior to testing efficacy. Another important
435 consideration is that the window of opportunity for Top1 inhibitor treatment in humans needs to
436 be carefully evaluated. Many reports indicate that the timing of the intervention against
437 Coronaviruses is key, as protective anti-viral and damaging excessive inflammatory responses
438 need to be balanced (Channappanavar et al., 2016; Channappanavar et al., 2019; Grajales-
439 Reyes and Colonna, 2020). Our data aligns with those studies, as early treatment of TPT did
440 not display protective effect in mice. In essence, limiting inflammatory response too early during
441 infection might increase viral replication and dissemination. As TPT-mediated inhibition of
442 inflammation could theoretically lead to a resurgence in viral replication, clinical trials will ideally
443 need to incorporate the administration of an anti-viral agent with activity against SARS-CoV-2
444 after TPT treatment. The safety and efficacy of our strategy will now be evaluated in two clinical
445 trials of TPT that have been submitted for trial initiation, and are set to begin in January 2021
446 (A.J, D.K., and I.M. *-personal communication*). Lastly, we strongly discourage any 'off label' use
447 of Top-1 inhibitors until safety and effectiveness is established by clinical trials.

448 449 **AUTHOR CONTRIBUTIONS**

450 Conceptualization: I.Marazzi
451 Investigation: J.S.Y.H., B.W.-Y.M., L.C., T.J., S.Y., S.P., J.A.W., N.N.G., D.A.M., S.V.I.,
452 I.Morozov, J.D.T., Y.S.F., R.R., Z.Z., S.Z., N.Z., B.S.M, H.R.-J., V.M., M.J.T., S.-Y.L., H.L.,
453 A.J.Z., A.C.-Y.L., W.-C.L., T.A.-G., A.M., R.A.A., M.Schotsaert, S.H.
454 Genomics analyses (Epigenetics): S.P., J.A.W., E.R.M., M.T.W.
455 Genomics analyses (Chromatin structure): S.H., C.B.
456 GSEA analysis: J.A.W., E.R.M.
457 Data analyses (Others): J.S.Y.H., Y.S.F., H.R.-J., V.M., M.Spivakov
458 In vivo study and veterinarian analysis: J.S.Y.H, B.W.-Y.M., L.C, S.-Y. L., H.L., A.J.Z., A.C.-Y.L.,
459 H.C., N.N.G., D.A.M., S.V.I., I.Morozov, J.D.T., J.A.R., M.C., U.B.R.B.
460 Histology and medical consultation: E.S., D.K., A.M., J.B., A.D.J.

461 Writing-Original draft: I.Marazzi
462 Resources: K.W., M.J.T., R.S., A.G.-S., B.R.T., S.K.C.
463 Writing-Review & Editing: J.S.Y.H, Z.Z., E.G., E.S., D.A.K., M.B., E.R.M., A.G.-S., M.T.W., S.H.,
464 C.B., J.A.R., I. Marazzi
465 Funding acquisition: A.G.-S., H.C., C.B., J.A.R., I. Marazzi
466 Project administration: I. Marazzi
467 Supervision: I. Marazzi

468

469 **ACKNOWLEDGEMENTS**

470 We thank the staff of KSU Biosecurity Research Institute, the histological laboratory at the
471 Kansas State Veterinary Diagnostic Laboratory (KSVDL), members of the Histology and
472 Immunohistochemistry sections at the Louisiana Animal Disease Diagnostic Laboratory
473 (LADDL), the CMG staff and Bianca Artiaga, Dashzeveg Bold, Konner Cool, Emily Gilbert-
474 Esparza, Chester McDowell and Yonghai Li. We thank the teams from the Genomics and
475 Mouse facilities at Icahn School of Medicine at Mount Sinai, the Global Health and Emerging
476 Pathogens Institute (GHEPI) at Mount Sinai. We thank Alan Soto from the Biorepository and
477 Pathology Dean's CoRE at the Icahn School of Medicine at Mount Sinai. We thank Cindy
478 Beharry, Sonia Jangra, Nanyi Julia Zhao, Nancy Francoeur, Nataly Fishman, Marion Dejeosez,
479 Thomas Zwaka and Carles Martinez-Romero for their help and advice.

480 This work was partially supported through grants from NBAF Transition Funds, the NIAID
481 Centers of Excellence for Influenza Research and Surveillance under contract number HHSN
482 272201400006C and the Department of Homeland Security Center of Excellence for Emerging
483 and Zoonotic Animal Diseases under grant no. HSHQDC-16-A-B0006 to JAR.

484 This work was partially supported by CRIP (Center for Research for Influenza Pathogenesis), a
485 NIAID supported Center of Excellence for Influenza Research and Surveillance (CEIRS,
486 contract # HHSN272201400008C) by supplements to NIAID grant U19AI135972 and DoD
487 grant W81XWH-20-1-0270, by the Defense Advanced Research Projects Agency (HR0011-19-
488 2-0020), and by the generous support of the JPB Foundation, the Open Philanthropy Project
489 (research grant 2020-215611 (5384) and anonymous donors to A.G.-S

490 This work was partially supported by funding to I.M., specifically the Burroughs Wellcome Fund
491 (United States; 1017892); the Chan Zuckerberg Initiative (United States; 2018-
492 191895), the Hirschl Young Investigator fellowship, the NIH UO1 0255-E051 and RO1 0255-
493 B641.

494

495 **COMPETING INTERESTS**

496 The García-Sastre Laboratory has received research support from Pfizer, Senhwa Biosciences,
497 7Hills Pharma, Pharmamar, Blade Therapeutics, Avimex, Johnson & Johnson, Dynavax, Kenall
498 Manufacturing and ImmunityBio. Adolfo García-Sastre has consulting agreements for the
499 following companies involving cash and/or stock: Vivaldi Biosciences, Contrafect, 7Hills
500 Pharma, Avimex, Vaxalto, Accurius and Esperovax. M.J.T. is an employee, and M.S. is a co-
501 founder of Enhanc3D Genomics Ltd. I.M. is an inventor in the patent, Serial Number:
502 16/063,009
503

504 **RESOURCE AVAILABILITY**

505

506 **Lead Contact**

507 Further information and requests for reagents may be directed to and will be fulfilled by Lead
508 Contact Ivan Marazzi (ivan.marazzi@mssm.edu).

509

510 **Materials Availability**

511 All unique/stable reagents generated in this study are available from the Lead Contact with a
512 completed Materials Transfer Agreement.

513

514 **EXPERIMENTAL MODEL AND SUBJECT DETAILS**

515

516 **Cells**

517 Human alveolar basal epithelial carcinoma cells (A549, ATCC CCL-185) and monkey kidney
518 epithelial cells (Vero E6, ATCC CRL-1586) were maintained at 37°C and 5% CO₂ and cultured
519 in Dulbecco's Modified Eagle's Medium (DMEM; Gibco) supplemented with 10% fetal bovine
520 serum (FBS; Gibco).

521

522 **Viral strains**

523 For infections in A549-ACE2 cells and K18-hACE2 mice, SARS-related coronavirus 2 (SARS-
524 CoV-2), isolate USA-WA1/2020 (NR-52281) was used (Blanco-Melo et al., 2020; Daniloski et
525 al., 2020). For Infections with hamsters in **Figure 3**, isolate HKG/13_P2/2020 (MT835140) was
526 used. For Infections with hamsters in **Figure S2**, isolate USA-WA1/2020 (NR-52281) was used.
527 SARS-CoV-2 was grown in Vero E6 cells in DMEM supplemented with 2% FBS, 4.5 g/L D-
528 glucose, 4 mM L-glutamine, 10 mM non-essential amino acids, 1 mM sodium pyruvate and 10
529 mM HEPES. Plaque assays were used to determine infectious titers of SARS-CoV-2 by
530 infection of Vero E6 cells in Minimum Essential Media supplemented with 2% FBS, 4 mM L-
531 glutamine, 0.2% BSA, 10 mM HEPES and 0.12% NaHCO₃ and 0.7% agar.

532

533 **METHOD DETAILS**

534

535 **Generation of A549-ACE2 Cells**

536 Generation of A549-ACE2 cells was performed as previously described (Blanco-Melo et al.,
537 2020; Daniloski et al., 2020). Briefly, A549 cells were transduced with lentiviral vector pHR-PGK
538 expressing human ACE2 coding sequence. A549 cells were then transduced with the lentivirus
539 in the presence of polybrene (8 µg/ml). Cells were used for downstream assays after 48h post
540 transduction.

541

542 **Preparation of siTOP1 sequencing libraries**

543 7.5E4 A549-ACE2 cells were plated in a 24 well dishes. 16 hours post plating, cells were
544 transfected with control, scrambled (siSCR), Top1-targeting (siTOP1) or no siRNA (no siRNA)
545 using Lipofectamine RNAiMax to a final concentration of 50nM. 48hours post transfection, the
546 media was replaced, and fresh media was added to each well. Cells were then mock infected
547 (PBS only) or infected with SARS-CoV-2 at MOI 0.5. 24 hours post infection, media was
548 removed, and cells were lysed in 250ul of Trizol reagent (Thermo Scientific). RNA was then
549 extracted using the Purelink RNA Minikit (Invitrogen) with DNaseI treatment, according to the
550 manufacturer's recommendations. RNA quality was determined using the RNA 6000 Nano kit
551 and the Eukaryote Total RNA Nano assay on the Agilent 2100 Bioanalyzer System. RNA
552 quantity was determined by Qubit™ RNA HS Assay Kit.

553

554 To then prepare RNA-sequencing libraries, 300 ng of RNA was depleted of ribosomal RNA
555 using NEBNext® rRNA Depletion Kit (Human/Mouse/Rat), according to the manufacturer's
556 instructions. Libraries were then prepared from rRNA depleted RNA using the NEBNext®
557 Ultra™ II Directional RNA Library Prep Kit for Illumina®, following the manufacturer's
558 instructions. Final libraries were quantified and sizing was determined using the High Sensitivity
559 DNA Assay reagents and chip in the Agilent 2100 Bioanalyzer System and the Qubit 1X dsDNA
560 HS Assay Kit respectively. Individual libraries were then pooled and sequenced using 75bp
561 paired end on the NextSeq 550 using the NextSeq 500/550 High Output Kit

562

563 **ChIP-Seq Library preparation**

564 To prepare ChIP-Sequencing libraries, ~2E5 A549-ACE2 cells were plated into 12 well dishes.
565 Cells were either mock infected (PBS only) or infected with SARS-CoV-2 virus at MOI 0.5. 24
566 hours post infection, media was removed from the well, and replaced with Fixation buffer (PBS,
567 2% FBS, 1% Methanol-Free Formaldehyde). Cells were fixed at room temperature for 10 min. 2M
568 Glycine was then added to a final concentration of 0.125M, and cells were incubated at room
569 temperature for 5min to quench the reaction. Supernatants were removed from wells, and each
570 well was washed 3 times with cold PBS. Cells were then lysed in the well using 250ul of SDS
571 Lysis Buffer [100mM NaCl, 50mM Tris pH8.0, 5mM EDTA, 0.02% NaN₃, 0.5% SDS + 1X Halt
572 Protease and Phosphatase Inhibitor (Thermo Scientific)] and cell lysates were collected in a
573 1.5ml tube and snap frozen at -80°C. On the day of sonication, lysates were thawed, and diluted
574 with 125ul of Triton Dilution Buffer [100mM Tris pH8.5, 100mM NaCl, 5mM EDTA, 0.02% NaN₃,
575 5% TritonX-100 + 1X Halt Protease and Phosphatase Inhibitor]. Lysates were then sonicated for
576 5 - 30 sec ON/ 30 sec OFF cycles twice using the Bioruptor Pico. Each sonicated lysate was
577 then pre-cleared using 10ul of Rabbit-IgG Dynabeads for 1 hour, rotating at 4°C. 1ug of anti-
578 H3K27ac antibody was then added to 300ul of pre-cleared lysate. Immunoprecipitation (IP) was
579 performed with overnight rotation at 4°C. To recover IP-complexes, 10ul of Dynabeads M-280
580 Sheep anti-Rabbit IgG were added to each reaction and tubes were rotated for 2 hours at 4°C.
581 Bead-chromatin complexes were then washed 6 times on a magnet using ice cold RIPA wash
582 buffer [50mM Hepes-KOH pH7.6, 100mM LiCl, 1mM EDTA, 1% NP-40, 0.5% Na-
583 Deoxycholate]. Washed beads were then incubated in 125ul Elution buffer [1% SDS, 0.1M
584 NaHCO₃] at 65°C overnight for elution and de-crosslinking. ChIP DNA was then purified using
585 the MinElute PCR purification kit (Qiagen) and quantified using the Qubit 1X dsDNA HS Assay
586 Kit.

587

588 ChIP libraries were prepared using the NEBNext® Ultra™ II DNA Library Prep Kit for Illumina
589 following the manufacturer's recommendations. 1ng of ChIP-DNA was used to prepare each
590 library. ChIP input libraries were prepared by pooling equal amounts of purified sonicated and
591 non-IPed DNA from each sample. 1ng of the pooled ChIP-input DNA was used for library
592 preparation. Libraries were quantified and sizing was determined using the High Sensitivity DNA
593 Assay reagents and chip in the Agilent 2100 Bioanalyzer System and the Qubit 1X dsDNA HS
594 Assay Kit respectively. Individual libraries were then pooled and sequenced 75bp paired end on
595 the NextSeq 550 using the NextSeq 500/550 High Output Kit v2.5.

596

597 **Preparation of HiC libraries**

598 In situ Hi-C was performed as described (Heinz 2018) with modifications. The day before
599 infection, 200k A549-ACE2 cells were plated in a 12 well dishes. Cells were either mock-
600 infected (PBS only) or infected with SARS-CoV-2 virus at MOI 0.5. Twenty-four hours post
601 infection, media was removed from the well, and replaced with Fixation buffer (PBS, 2% FBS,
602 1% Methanol-Free Formaldehyde). Cells were fixed at room temperature for 10 min. 2M Glycine
603 was then added to a final concentration of 0.125M, and cells were incubated at room
604 temperature for 5min to quench the reaction. Supernatants were then removed wells, and each

605 well was washed 2 times with cold PBS. Cells were then lysed in the well using 250 μ l of Lysis
606 Buffer [0.5% SDS + Halt Protease and Phosphatase Inhibitors (Thermo Scientific)]. Cell lysates
607 were collected in a 1.5ml tube. 1.5 mU RNaseA (Thermo Scientific) was added to each lysate,
608 and lysates were then incubated at 37°C for 1h. RNaseA treated lysates were then snap frozen
609 and stored in -80°C. After thawing, nuclei were collected at 1500 g for 5 minutes at room
610 temperature. Most of the supernatant was discarded, leaving the nuclei in 10 μ l liquid. Samples
611 were resuspended in reaction buffer (25 μ l 10% Triton X-100, 25 μ l 10x Dpn II buffer, 188 μ l
612 water) and rotated at 37°C, 8 RPM for 15 minutes. Chromatin was digested overnight (ON) with
613 either 2 μ l (100 U) Dpn II (NEB) (later experiments) at 37°C, rotating overhead with 8 RPM.
614 Nuclei were collected by centrifugation at 1500 g for 5 minutes at room temperature, 225 μ l of
615 the supernatant were discarded, leaving the nuclei in 25 μ l liquid, and overhangs were filled in
616 with Biotin-14-dATP by adding 75 μ l Klenow Master Mix (54.45 μ l water, 7.5 μ l NEBuffer 2, 0.35
617 μ l 10 mM dCTP, 0.35 μ l 10 mM dTTP, 0.35 μ l 10 mM dGTP, 7.5 μ l 0.4 mM Biotin-14-dATP
618 (Invitrogen), 2 μ l 10% Triton X-100, 2.5 μ l (12.5 U) Klenow fragment (Enzymatics)) and rotating
619 overhead at RT, 8 RPM for 40 minutes. Reactions were stopped by adding 2.5 μ l 0.5 M EDTA
620 and placed on ice. Proximity ligation was performed by transferring the entire reaction into 1.5
621 ml Eppendorf tubes containing 400 μ l ligase mix (322.5 μ l water, 40 μ l 10x T4 DNA ligase buffer
622 (Enzymatics), 36 μ l 10% Triton X-100, 0.5 μ l 10 % BSA, 1 μ l (600 U) T4 DNA ligase (HC,
623 Enzymatics) and rotating ON at 16°C, 8 RPM. Reactions were stopped with 20 μ l 0.5 M EDTA,
624 treated with 1 μ l 10 mg/ml DNase-free RNase A for 15 minutes at 42°C, then 31 μ l 5 M NaCl,
625 29 μ l 10 % SDS and 5 μ l 20 mg/ml DNase-free proteinase K (Thermo) were added, proteins
626 digested for 1 h at 55°C while shaking at 800 RPM, then crosslinks reversed ON at 65°C. After
627 extraction with 600 μ l pH 8-buffered phenol/chloroform/isoamyl alcohol (Ambion) followed by
628 extraction with 600 μ l chloroform, DNA was precipitated with 1.5 μ l (22.5 μ g) Glycoblue
629 (Ambion) and 1400 μ l 100% ethanol ON at -20°C. After centrifugation for 20' at 16000g, 4°C,
630 the DNA pellet was washed twice with 80% ethanol, and the pellet air-dried and dissolved in
631 131 μ l TT (0.05% Tween 20/Tris pH 8). DNA (200 ng) was sheared to 300 bp in 130 μ l TT on a
632 Covaris E220 sonicator using the manufacturer's protocol. Biotinylated DNA was captured on
633 Dynabeads MyOne Streptavidin T1 (Thermo) by combining the sonicated DNA sample (130 μ l)
634 with 20 μ l Dynabeads that had previously been washed with 1x B&W buffer (2X B&W: 10 mM
635 Tris-HCl pH=7.5, 1 mM EDTA, 2 M NaCl) and had been resuspended in 130 μ l 2x B&W
636 containing 0.2% Tween 20. The binding reaction was rotated at RT for 45 minutes, and DNA-
637 bound beads were vigorously washed twice with 150 μ l 1x B&W/0.1% Triton-X 100, once with
638 180 μ l TET (0.05% Tween 20, 10 mM Tris pH 8, 1 mM EDTA). Libraries were prepared on-
639 beads using an NEBnext Ultra II DNA library prep kit using half the reagent/reaction volumes
640 given in NEB's instruction manual and 1.6 pmol Bioo DNA sequencing adapters (Illumina
641 TruSeq-compatible) per reaction. Reactions were stopped by adding 5 μ l 0.5 M EDTA, beads
642 collected on a magnet and washed twice with 150 μ l 1x B&W/0.1% Triton-X 100, twice with 180
643 μ l TET and resuspended in 20 μ l TT (0.05% Tween 20, 10 mM Tris pH 8.0). Libraries were
644 amplified by PCR for 10 cycles (98°C, 30s; 10x [98°C, 10s; 63°C, 20s; 72°C, 30s]; 72°C, 2 min;
645 4°C, ∞), using 10 μ l of the bead suspension in a 50 μ l reaction with NEBNext Ultra II Q5 2x
646 master mix (NEB) and 0.5 μ M each Solexa 1GA/1GB primers (Solexa 1GA:
647 AATGATACGGCGACCACCGA, Solexa 1GB: CAAGCAGAAGACGGCATACTGA). Libraries
648 were precipitated onto magnetic beads by adding 40 μ l 20% PEG8000/2.5 M NaCl and 2 μ l
649 SpeedBeads (8.9 % PEG final) to 48 μ l PCR reaction, thorough mixing by vortexing followed by
650 10-minute incubation at RT. Beads were collected using a magnet and the supernatant
651 discarded. After washing beads twice by adding 180 μ l 80% EtOH, moving the tube strip 6x
652 from side to side of the magnet, collecting beads and discarding the supernatant, beads were
653 air-dried, and DNA eluted by adding 20 μ l TT. Libraries were sequenced paired-end for 42
654 cycles each to a depth of approximately 250 million reads per experiment on an Illumina
655 NextSeq 500 sequencer.

656
657
658
659
660
661
662
663
664
665
666
667
668
669
670
671
672
673
674
675
676
677
678
679
680
681
682
683
684
685
686
687
688
689
690
691
692
693
694
695
696
697
698
699
700
701
702
703
704
705

Preparation of Hamster RNA sequencing libraries

For RNA sequencing analyses in infected hamsters shown in **Figure 3**, infected hamsters that were treated with TPT or vehicle control, were euthanized at days 4 and 6 post infection. Uninfected hamsters were used as controls. After euthanasia, lung left inferior lobe from hamsters were cut into pieces and lysed with RA1 lysis buffer provided with the *NucleoSpin® RNA Plus* kit (Macherey-nagel), RNA extraction was performed according the manufacturer's recommendations, including an on-column genomic DNA digestion step. RNA sequencing library preparation and sequencing were then performed by BGI Genomics

Hamster Infections

For experiments shown in **Figure 3**, Female Golden Syrian hamster, aged 6-8 week old (~70-100g), were obtained from Laboratory Animal Unit, University of Hong Kong (HKU). All experiments were performed in a Biosafety Level-3 animal facility, LKS Facility of Medicine, HKU. The study has been approved by the Committee on the Use of Live Animals in Teaching and Research, HKU. Virus stock was diluted with Phosphate-buffered saline (PBS) to 2×10^4 PFU/ml. Hamsters were anesthetized with ketamine (150mg/kg) and xylazine (10 mg/mg) and then intranasally inoculation with 50 ul of diluted viruses containing 10^3 PFU of viruses. For drug treatments, 10mg/kg TPT resuspended in vehicle [5% DMSO + 5% corn oil in PBS] or vehicle alone was administered intraperitoneally to animals on the indicated days post infection.

For experiments shown in **Figure S2**, infection procedures were performed following protocols approved by the Icahn School of Medicine at Mount Sinai Institutional Animal Care and Use Committee (IACUC). Animal studies were carried out in strict accordance with the recommendations in the Guide for the Care and Use of Laboratory Animals of the National Research Council. 7-10 week old (~120-140g) female Golden Syrian hamsters (Charles River) were anesthetized using 90mg/kg Ketamine and 2mg/kg Xylazine by intraperitoneal injection. Once anesthetized, hamsters were intranasally infected with $1E5$ PFU of SARS-CoV-2 virus resuspended in 100ul of PBS. Animals were monitored daily for clinical signs of illness and weight loss after infection. For drug treatments, 2mg/kg TPT resuspended in vehicle [4.5% DMSO + 20% Sulfobutylether- β -Cyclodextrin (SBE- β -CD) in PBS] or vehicle alone was administered intraperitoneally to animals on the indicated days post infection.

K18-hACE2 mice infections

All mice infection procedures were performed following protocols approved by the Icahn School of Medicine at Mount Sinai Institutional Animal Care and Use Committee (IACUC). Animal studies were carried out in strict accordance with the recommendations in the Guide for the Care and Use of Laboratory Animals of the National Research Council. 5-10 week old female B6.Cg-Tg(K18-ACE2)2PrImn/J (K18-hACE2) mice purchased from Jackson Laboratories (Bar Harbor, ME) were anesthetized by an intraperitoneal injection of 90mg/kg Ketamine and 2 mg/kg xylazine. Once anesthetized, mice were infected with $1E4$ PFU of SARS-CoV-2 virus suspended in 30ul of PBS. Mice were monitored daily for clinical signs of illness and weight loss after infection. Animals that reached 75% bodyweight or clinical signs that are irrevocably linked with death were humanely euthanized by intraperitoneal injection of 60mg/kg pentobarbital.

For drug treatments, 2mg/kg Topotecan-hydrochloride (TPT; 14129, Cayman Chemical Company) re-suspended in vehicle [4.5% DMSO + 20% Sulfobutylether- β -Cyclodextrin (SBE- β -CD) in PBS] was administered intraperitoneally to animals on the indicated days post infection.

Extraction of RNA from Lungs of Infected Hamsters and Mice

706 Upon euthanasia, the superior lobe of infected hACE2-KI mice or Golden Syrian hamsters were
707 collected for RNA extraction. Lungs were lysed and homogenized in Trizol. RNA extraction was
708 performed using the Purelink RNA Mini Kit with a DNaseI treatment step, according to the
709 manufacturer's recommendations. cDNA was synthesized from RNA using the High-Capacity
710 cDNA Reverse Transcription Kit (ThermoFisher).

711
712 **Histological analysis**
713 For histological slides shown in **Figure 3E to 3H**, Lung left superior lobes of infected Golden
714 Syrian hamster were fixed in 4 % paraformaldehyde and then processed for paraffin
715 embedding. The 4µm tissue sections were stained with haematoxylin and eosin for
716 histopathological examination. Images were with Olympus BX53 semi-motorized fluorescence
717 microscope using cellSens imaging software.

718 For histological slides shown in **Figure S2D and S2E**, the left lung lobe of infected Golden
719 Syrian hamsters was fixed in 10% formalin for 48 hours. Embedding in paraffin blocks and
720 staining with H&E were conducted by the Biorepository and Pathology Dean's CoRE at the the
721 Icahn School of Medicine at Mount Sinai. Microscopic sections were analyzed in a blinded
722 fashion by the same pathologist (A.M.). A number was randomly assigned by the investigator to
723 discriminate each section, which was then submitted for analysis. No information about
724 treatments and mouse genotypes was communicated to the pathologist. Lungs were scored by
725 the area involved in broncho-pneumonia.

726
727

728 **QUANTIFICATION AND STATISTICAL ANALYSES**

729 **Mouse Infection Studies**

730 Mice were randomly assigned into treatment groups. Statistical significance between survival
731 curves was calculated using a Log-rank (Mantel-Cox) test using Graphpad Prism 8.0 software.
732 Two tailed Student's t-tests under the assumption of equal variances between groups were
733 used to compare weight loss in mice from different groups for each day post infection. Data are
734 shown as +-SEM.

735
736 **Quantitative qPCR assays**
737 qPCR assays were done with 3-4 biological replicates (3-4 infected animals/condition).
738 Statistical significance in gene expression was estimated with Graphpad Prism 8.0 software,
739 and determined using two-tailed Student's t test under the assumption of equal variances
740 between groups. Data are shown as +/- SEM

741
742 **Illumina Short Read RNA sequencing analyses**
743 After adaptor removal with cutadapt (Martin, 2011) and base-quality trimming to remove 3' read
744 sequences if more than 20 bases with Q <20 were present, paired-end reads were mapped to
745 the SARS-CoV-2 and human (hg38) or hamster (*Mesocricetus auratus*; MesAur1.0) reference
746 genomes with STAR . Gene-count summaries were generated with featureCounts (Liao et al.,
747 2014). A numeric matrix of raw read counts was generated, with genes in rows and samples in
748 columns, and used for differential gene expression analysis with the Bioconductor Limma
749 package (Ritchie et al., 2015) after removing genes with less than 50 total reads across all
750 samples or of less than 200 nucleotides in length. Normalization factors were computed on the
751 filtered data matrix using the weighted trimmed mean of M-values (TMM) method, followed by
752 voom (Law et al., 2014) mean-variance transformation in preparation for Limma linear modeling.
753 To specifically identify the effect of siRNA mediated Top1 depletion on the inflammatory
754 responses to SARS-CoV-2 in A549-ACE2 cells shown in **Figure 2**, we used interaction model
755 (siTOP1_Infected:siTOP_uninfected - siSCR_Infected:siSCR_uninfected or
756 no_siRNA_infected:no_siRNA_uninfected - siSCR_Infected:siSCR_uninfected), that takes into

757 account basal differences between conditions. To identify TPT dependent gene expression
758 changes in infected hamsters shown in **Figure 3**, we performed pairwise contrast between
759 experimental groups (i.e: TPT D4 – DMSO D4; TPT D6 – DMSO D6). Pairwise comparisons
760 were then performed between treatment groups and eBayes adjusted P-values were corrected
761 for multiple testing using the Benjamin-Hochberg (BH) method and used to select genes with
762 significant expression differences (fold change > 1.5, adjusted P value <0.05).

763
764 **GSEA analysis for gene signatures in TPT treated hamsters**
765 We identified Top1 inhibitor gene signatures from TPT-treated Syrian hamsters infected with
766 SARS-CoV-2. We defined the up- and down-regulated signatures as genes differentially
767 expressed after 4 or 6 days of treatment ($\log_2|FC| > 1$, FDR=10%). We converted hamster
768 genes to available human orthologs using ENSEMBL (Release 101). We downloaded
769 normalized transcript expression from targeted RNA-seq (398 genes) on lung autopsy tissue
770 from COVID19 patients (16 patients, 34 samples), normal lung tissue (6 patients, 17 samples),
771 and lung tissue from bacterial or viral pneumonia (4 patients, 5 samples) [(Nienhold et al.,
772 2020), GEO accession: GSE151764]. Gene set enrichment analysis (Subramanian et al., 2005)
773 was performed using the R package fgsea (Korotkevich et al., 2019). We used Tukey's multiple
774 comparison test to identify significant differences in mean normalized enrichment scores.

775
776 **ChIP-seq analysis**
777 ChIP-seq datasets were processed and analyzed using an in-house automated pipeline
778 (<https://github.com/MarioPujato/NextGenAligner>). Briefly, basic quality control for raw
779 sequencing reads was performed using FASTQC (version 0.11.2)
780 (<http://www.bioinformatics.babraham.ac.uk/projects/fastqc>). Adapter sequences were removed
781 using Trim Galore (version 0.4.2)
782 (https://www.bioinformatics.babraham.ac.uk/projects/trim_galore/), a wrapper script that
783 runs cutadapt (version 1.9.1) to remove the detected adapter sequence from the reads. The
784 quality controlled reads were aligned to the reference human genome (hg19/GRCh37) using
785 bowtie2 (version 2.3.4.1)(Langmead and Salzberg, 2012). Aligned reads were then sorted using
786 samtools (version 1.8)(Li et al., 2009) and duplicate reads were removed using picard (version
787 1.89) (<https://broadinstitute.github.io/picard/>). Peaks were called using MACS2 (version 2.1.0)
788 (<https://github.com/taoliu/MACS>)(Zhang et al., 2008) with the control/input aligned reads as
789 background (callpeak -g hs -q 0.01 –broad -c input/control). ENCODE blacklist regions
790 (Amemiya et al., 2019) were removed using the hg19-blacklist.v2.bed.gz file available at
791 <https://github.com/Boyle-Lab/Blacklist/tree/master/lists>.

792
793 The ChIP-seq experimental design consisted of triplicates experiments for each condition (0hr,
794 8hr, 24hr infections). PCA analysis indicating strong agreement between experimental
795 replicates and clear separation between conditions (**Figure S1A**) Sequencing reads from
796 replicates were thus combined, and alignment and peak calling was again performed as
797 described above. For differential peak analysis, the union set of all peaks from these three
798 conditions was generated using bedtools (Quinlan and Hall, 2010). For each of the resulting
799 genomic regions, read counts were obtained for all 9 replicates. These read counts used as
800 input to DESeq2 (Love et al., 2014). A fold change cutoff of greater than or equal to 1.5 and an
801 FDR-corrected p-value cutoff of less than or equal to 0.05 were used to identify differential
802 peaks for each pairwise comparison between conditions.

803
804 We used the HOMER suite of tools (Heinz et al., 2010), modified to use a log base two scoring
805 system and to include the large set of human motifs contained in the CisBP database (build
806 2.0)(Lambert et al., 2019) to identify enriched motifs within the sequences of differential and
807 shared ChIP-seq peaks. To minimize redundancy, motifs were grouped into classes using the

808 following procedure. Each human transcription factor was assigned the single best p-value
809 obtained for any of its corresponding motifs. Transcription factors with identical best motifs
810 were merged then into a single class.

811

812 **HiC analysis**

813 Hi-C data was processed as described in (Heinz et al., 2018). Briefly, Hi-C reads were trimmed
814 at Mbol/DpnII recognition sites (GATC) and aligned to the human genome (GRCh38/hg38)
815 using STAR (Dobin et al., 2013), keeping only read pairs that both map to unique genomic
816 locations for further analysis (MAPQ > 10). All PCR duplicates were also removed. PCA
817 analysis of Hi-C experiments used to define chromatin compartments were performed with
818 HOMER(Lin et al., 2012). For each chromosome, a balanced and distance normalized contact
819 matrix was generated using window size of 50 kb sampled every 25 kb, reporting the ratios of
820 observed to expected contact frequencies for any two regions. The correlation coefficient of the
821 interaction profiles for any two regions across the entire chromosome were then calculated to
822 generate a correlation matrix (also visualized in **Figure 1A**). This matrix was then analyzed
823 using Principal Component Analysis (PCA) from the prcomp function in R ([https://www.r-](https://www.r-project.org)
824 [project.org](https://www.r-project.org)), and the eigenvector loadings for each 25 kb region along the first principal
825 component were assigned to each region (PC1 values). The PC1 values from each
826 chromosome were scaled by their standard deviation to make them more comparable across
827 chromosomes and analysis parameters. For each chromosome, PC1 values are multiplied by
828 -1 if negative PC1 regions are more strongly enriched for active chromatin regions defined by
829 H3K27ac peaks to ensure the positive PC1 values align with the A/permissive compartment (as
830 opposed to the B/inert compartment). chrY was excluded from the PCA analysis due to its small
831 size and high repeat content. Balanced, normalized Hi-C contact maps were generated at 25 kb
832 resolution for visualization (**Figure 1A**). Assignment of PC1 values to Gencode gene promoters
833 and other features was performed using HOMER's annotatePeaks.pl function using the results
834 from the PCA analysis.

835

836

837 **FIGURE LEGENDS**

838

839 **Figure 1: SARS-CoV-2 restructures chromatin in host cells.**

840 **(A) Upper panel:** Analysis of 3D chromatin structure in SARS-CoV-2 infected and control A549-
841 ACE2 cells by Hi-C. Normalized Hi-C contact matrices are shown for the uninfected (0hpi)
842 control (lower-left) and 24 hours post infection (hpi, upper-right) for a representative 30 Mb
843 region of chromosome 9. White rectangles highlight regions with strong changes in interaction
844 patterns between conditions. **Middle panel:** pairwise correlation matrices for uninfected control
845 and 24 hpi Hi-C experiments analysis for the same region shown in the upper panel. **Lower**
846 **panel:** PC1 values, which represent the PCA loadings describing the chromatin compartment
847 membership (+ values for the A compartment, - values for the B compartment) are show along
848 with H3K27ac ChIP-seq levels for the region depicted. Cells infected for 24 hours show
849 increased segregation of chromatin into smaller A and B compartment domains.

850 **(B)** Distribution of A and B compartment domain sizes genome wide for uninfected control and
851 24 hpi A549-ACE2 cells.

852 **(C)** Scatter plot comparing the PC1 values for every 25 kb region in the genome for uninfected
853 control and infected cells (8, 24 hpi). Data points colored red or blue indicate that they overlap
854 with a significantly regulated H3K27ac peaks (4-fold, adjusted p-value < 0.05).

855 **(D)** Distribution of the change in PC1 values between uninfected and 24 hpi at the promoters of
856 genes that are either expressed in A549-Ace2 cells, induced, or repressed by SARS-CoV-2
857 infection (>1.5-fold, adjusted p-value < 0.05).

858

859 **Figure 2: TOP1 depletion in SARS-CoV-2 infected cells inhibits induction of inflammatory** 860 **genes.**

861 **(A)** PCA plot showing the relationship between samples and treatment conditions.

862 **(B)** Heat map showing relative changes in gene expression levels in no siRNA (no siRNA) or
863 siTop1 (siTOP1) treated cells, when compared to nontargeting control siRNA-treated (siSCR)
864 cells. Shown are genes that are differentially expressed between siTOP1 and siSCR samples
865 (adjusted p-value < 0.05, fold change>1.5).

866 **(C)** Gene ontology analyses of downregulated target genes shown in (B).

867 **(D)** qPCR validation of select target genes shown in (B). Shown are the mean and s.d of 3
868 replicates. *: p<0.05; **: p<0.01 by two-tailed, unpaired Students' t-test.

869 **(E)** Barplots showing changes in gene expression levels upon SARS-CoV-2 infection, as
870 quantified by RNA seq, for all expressed genes (Exp), Top1 dependent induced genes (Dep)
871 and Top1-independent induced genes (Indep)

872 **(F)** Violin plots showing changes in PC1 (delta PC1) for 8 hours (8hpi) and 24 hours (24hpi)
873 post infection at expressed genes (Exp), Top1 dependent induced genes (Dep) and Top1-
874 independent induced genes (Indep). Horizontal lines indicate the means.

875 **(G)** Violin plots showing changes in H3K27ac levels (delta H3K27ac) for 8 hours (8hpi) and 24
876 hours (24hpi) post infection at expressed genes (Exp), Top1 dependent induced genes (Dep)
877 and Top1-independent induced genes (Indep). Horizontal lines indicate the means.

878

879 **Figure 3: TPT treatment reduces inflammatory gene expression in SARS-CoV-2 infected** 880 **hamsters**

881 **(A)** Schematic showing the infection and treatment regime used.

882 **(B)** PCA plot showing the relationship between treatment and infection groups.

883 **(C)** Heatmap showing gene expression levels of genes that are dysregulated with TPT
884 treatment in Uninfected (Green), DMSO (red and purple) or TPT treated (blue and yellow)
885 hamsters at days 4 and 6 post infection. Each column represents an individual hamster, and
886 each row represents one gene. Data are clustered by genes that are up- (yellow) or down-
887 (pink) regulated with infection with reference to the uninfected animals.

888 **(D)** Gene ontology analysis of genes that are down regulated with TPT treatment at days 4 (top)
889 and 6 (bottom) post infection
890 **(E)** Representative scan of hematoxylin and eosin (H&E) stained sections of the lungs of
891 infected hamsters that have been treated with DMSO 4 days post infection. Arrow: Diffuse lung
892 inflammatory damages. Bronchiolar epithelium cells death, bronchiolar luminal secretion and
893 hemorrhage; Arrowheads: Diffuse alveoli destruction with massive immune cell infiltration and
894 exudation; Open arrows: Vasculitis
895 **(F)** Representative scan of hematoxylin and eosin (H&E) stained sections of the lungs of
896 infected hamsters that have been treated with DMSO 6 days post infection. Lung tissue
897 consolidation affected most of the lung lobe examined. Bronchial secretion, infiltration and
898 alveolar space exudation, immune cell infiltration and hemorrhage are still present at this stage
899 (arrowheads), and is accompanied by alveolar and bronchiolar cell proliferation (arrows)
900 **(G)** Representative scan of hematoxylin and eosin (H&E) stained sections of the lungs of
901 infected hamsters that have been treated with TPT 4 days post infection. Diffuse milder
902 inflammatory damages. Arrows: Bronchiolar epithelium cells death with milder peribronchiolar
903 infiltration; Arrowheads: Diffuse alveolar wall thickening with capillary congestion. No
904 conspicuous alveolar space infiltration, exudation or hemorrhages; Open arrows: Vasculitis is
905 very mild and rare
906 **(H)** Representative scan of hematoxylin and eosin (H&E) stained sections of the lungs of
907 infected hamsters that have been treated with TPT 6 days post infection. Patchy lung tissue
908 consolidation with cell proliferation. Most alveolar area are without exudation and infiltration.
909 Bronchiolar luminal secretion is reduced compared to the with DMSO control.

910
911 **Figure 4: TPT suppresses gene programs upregulated in autopsy-lung from COVID19**
912 **patients.**

913 **(A)** Gene set enrichment analysis of lung-tissue gene expression profiles from COVID19
914 deceased patients versus healthy patients (Nienhold et al., 2020). Signed $-\log_{10}$ adjusted P
915 values indicate enrichment of down-regulated (top panel) and up-regulated (bottom panel) gene
916 signatures from TPT-treated hamsters infected with SARS-CoV-2. The sign of enrichment is
917 given by the normalized enrichment score (NES). Dashed lines indicate a significance levels of
918 $P=0.05$. Differences in mean NES are shown: * $P = 10^{-3}$, ** $P = 5 \times 10^{-4}$, *** $P = 10^{-7}$.
919 **(B)** Expression in lung autopsy tissue of COVID19 patients and healthy controls [(Nienhold et
920 al., 2020), GSE151764] of genes down-regulated in TPT-treated Sars-CoV-2-infected hamsters
921 ($\log_2|FC| > 1$, FDR=10%). Patient groups are indicated by the topmost bar, where healthy
922 controls are colored in cyan, and COVID-19 patients colored in red. Gene set enrichment
923 scores, calculated as $-\log_{10}(P) \cdot \text{sign}(\text{NES})$ are indicated in the middle bar. The sign of
924 enrichment is given by the normalized enrichment score (NES). Positive, higher scores (orange)
925 indicate that TPT-inhibited genes are more upregulated in a given patient, whereas negative,
926 lower scores (green) indicate that TPT-inhibited genes are more downregulated in a given
927 patient. The lower heatmap shows the individual gene expression profile of the indicated TPT-
928 inhibited gene for a given patient (in columns). Heatmap is sorted by column from the highest
929 (left) to lowest enrichment score (right).

930
931 **Figure 5: Late treatment of TPT in K18-hACE2 mice provides survival benefit during**
932 **SARS-CoV-2 infection.**

933 **(A)** Schematic showing infection and treatment regime in mice. Groups are color coded by
934 treatment regime
935 **(B)** Survival curve of K18-hACE2 mice infected with $1E4$ PFU of SARS-CoV-2 and
936 subsequently subjected to the indicated TPT treatment regimes. Number of mice used are
937 indicated in the legend. Blue: DMSO vehicle control only (n=9); Red: TPT 2mg/kg on Days 1

938 and 2 post infection (n=10); Green: TPT 2mg/kg on Days 3 and 4 post infection (n=10); Purple:
939 TPT 2mg/kg on Days 4 and 5 post infection (n=5).
940 **(C)** Weight loss curves in surviving mice shown in B. Numbers of mice at the end and start
941 (end/start) points of the experiment are indicated in the legend keys. Weights are shown as
942 means of the percentage of starting weights. Error bars show the SEM of each group. Blue:
943 DMSO only; Red: TPT 2mg/kg on Days 1 and 2 post infection; Green: TPT 2mg/kg on Days 3
944 and 4 post infection; Purple: TPT 2mg/kg on Days 4 and 5 post infection.
945 **(D)** qPCR of inflammatory gene expression for mice in the indicated treatment groups at day 7
946 post infection with 1E4 PFU SARS-CoV-2. Each dot represents an individual mouse. Lines
947 indicate the mean of expression.
948
949

950 **SUPPLEMENTARY FIGURE LEGENDS**

951

952 **Figure S1: H3K27ac profiles in SARS-CoV-2 infected A549-ACE2 cells**

953 Differential H3K27ac across infection time points. H3K27ac ChIP-seq peaks were classified
954 across the infection time course into clusters by their pattern of occurrence (see Methods).

955 (A) Principle Component (PCA) analysis of ChIP-seq experimental replicates. PCA was
956 performed across the genome using the set of peaks identified in each experimental replicate.
957 Percentage of variance explained by the first two components is shown along the axes. PCA
958 was performed using scikit-learn (Pedregosa et al., 2011).

959 (B) Venn diagram schematic depicting the seven possible patterns of peak occurrence (i-vii),
960 along with the number of peaks observed for each pattern at 0, 8 and 24 hours post infection.

961 (C) Heatmap indicating the normalized read count intensity within each peak for each of the
962 three timepoints, for the indicated clusters described in (B).

963 (D) Transcription factor binding site motif enrichment for each of the clusters shown in (B) and
964 (C). Motif enrichment was calculated within H3K27ac-marked regions. Bar plots indicate the
965 negative log p-value of enrichment for the top 100 motif classes (see Methods). Bars are
966 colored by motif. AP-1: Yellow; IRF: Green; NFkB: Red; STAT: Blue; Other: Grey

967

968 **Figure S2: Reduced TPT dosages have similar beneficial effects in SARS-CoV-2 infected hamsters.**

969 (A) Schematic showing infection and treatment regime in 7-10 week old hamsters.

971 (B) Lung weight to body weight ratios of Hamsters infected with 1E4 PFU SARS-CoV-2 at Day 4
972 post infection, and treated with either DMSO (red) or 2mg/kg TPT (blue). Each dot represents
973 an individual animal, and lines indicate the mean of Lung/Body weight ratios.

974 (C) Scatter plots depicting the percent of lung area that is involved in Broncho Pneumonia, as
975 blindly scored by the pathologist (A.M). Each dot represents an individual animal, and the lines
976 indicate the mean.

977 (D,E) Representative H&E sections of the left lung lobe of infected hamsters at day 4 post
978 infection, and treated either with DMSO (D) or 2mg/kg TPT (E) . Scale bar: 250uM.

979 (F) Inflammatory gene expression in DMSO or TPT infected hamsters at day 4 post infection.
980 Bars show the mean and SEM of 4 animals.

981

982

983 **SUPPLEMENTARY TABLE LEGENDS**

984
985 **Table S1: Table of HiC peak scores and their overlap with H3K27ac peaks (Related to**
986 **Figure 1)**

987 Table of processed Hi-C data used to derive panels shown in **Figure 1**. Abbreviations used:
988 IFC: interchromosomal interaction changes; DLR: distal/local ratio changes; Combo:
989 Replicates combined. Columns T-V: H3K27ac levels in region, at the indicated time points;
990 Columns W-AE: PC1 levels of combined or individual Hi-C replicates; Columns AF-AI: ICF and
991 DLR changes in indicated regions and for the specified contrasts; Column AJ-AQ: Significance
992 values for comparing PC1 values between conditions. Detailed Column descriptions are as
993 follows

994
995 **Table S2: H3K27ac ChIP-seq QC summary and differential peak analyses (Related to**
996 **Figure S1)**

997 Table S2A: QC analysis and statistics of H3K27ac ChIP-seq data

998 Table S2B: Full results of H3K27ac differential peak analysis (Contrast 8h vs 0h)

999 Table S2C: Full results of H3K27ac differential peak analysis (Contrast 24h vs 0h)

1000

1001 **Table S3: H3K27ac ChIP-seq transcription motif analyses summary**

1002 Full results of transcription factor binding site motif enrichment analysis.

1003

1004 **Table S4: Differential expression analysis (RNA-seq) for siRNA treated infected A549-**
1005 **ACE2 cells (Related to Figure 2)**

1006 **Table S4A:** Fold change and associated significance values for genes that are differentially
1007 expressed (Fold change > 1.5, p.adj < 0.05) in siTOP1 cells when compared to siSCR treated
1008 cells.

1009 **Table S4B:** Same genes shown in Table S4A, but showing the fold changes and associated
1010 significance values for in no siRNA treated (no siRNA) cells when compared to siSCR treated
1011 cells.

1012 **Table S4C:** Gene lists for all expressed, Top1 dependent and Top1 independent genes. Shown
1013 are the log₂FC, AveExpr, t-stat, p-values, adjusted p-values and B-stats for the siSCR infected
1014 vs siSCR uninfected contrast, used to define infection induced genes. Genes that are induced
1015 by infection are indicated by “1” in Column I. Genes that are Top1 dependent and induced by
1016 infection are indicated by “1” in Column J. Genes that are Infection induced and Top1
1017 independent are indicated by “1” in Column K.

1018

1019 **Table S5: Gene ontology (pathway) analyses (Related to Figure 2C)**

1020 Gene ontology pathway analysis for downregulated genes listed in Figure 2B and Tables S4.

1021

1022 **Table S6: Blind scores of lung sections from TPT and vehicle (DMSO) treated SARS-CoV-**
1023 **2 Hamsters (Related to Figure S2D and S2E)**

1024 Scoring of H&E stained lung sections taken from hamsters infected with SARS-CoV-2 and
1025 treated with vehicle (DMSO) or 2mg/kg TPT at days 1 and 2 post infection. Lung sections were
1026 isolated on day 4 post infection.

1027

1028 **REFERENCES**

- 1029 Amemiya, H.M., Kundaje, A., and Boyle, A.P. (2019). The ENCODE Blacklist: Identification of
1030 Problematic Regions of the Genome. *Sci Rep* *9*, 9354.
- 1031 Andre, T., Louvet, C., Maindrault-Goebel, F., Couteau, C., Mabro, M., Lotz, J.P., Gilles-Amar,
1032 V., Krulik, M., Carola, E., Izrael, V., *et al.* (1999). CPT-11 (irinotecan) addition to bimonthly,
1033 high-dose leucovorin and bolus and continuous-infusion 5-fluorouracil (FOLFIRI) for pretreated
1034 metastatic colorectal cancer. *GERCOR. Eur J Cancer* *35*, 1343-1347.
- 1035 Banerjee, A.K., Blanco, M.R., Bruce, E.A., Honson, D.D., Chen, L.M., Chow, A., Bhat, P.,
1036 Ollikainen, N., Quinodoz, S.A., Loney, C., *et al.* (2020). SARS-CoV-2 Disrupts Splicing,
1037 Translation, and Protein Trafficking to Suppress Host Defenses. *Cell*.
- 1038 Bao, L., Deng, W., Huang, B., Gao, H., Liu, J., Ren, L., Wei, Q., Yu, P., Xu, Y., Qi, F., *et al.*
1039 (2020). The pathogenicity of SARS-CoV-2 in hACE2 transgenic mice. *Nature* *583*, 830-833.
- 1040 Bhatraju, P.K., Ghassemieh, B.J., Nichols, M., Kim, R., Jerome, K.R., Nalla, A.K., Greninger,
1041 A.L., Pipavath, S., Wurfel, M.M., Evans, L., *et al.* (2020). Covid-19 in Critically Ill Patients in the
1042 Seattle Region - Case Series. *N Engl J Med* *382*, 2012-2022.
- 1043 Blanco-Melo, D., Nilsson-Payant, B.E., Liu, W.C., Uhl, S., Hoagland, D., Moller, R., Jordan,
1044 T.X., Oishi, K., Panis, M., Sachs, D., *et al.* (2020). Imbalanced Host Response to SARS-CoV-2
1045 Drives Development of COVID-19. *Cell* *181*, 1036-1045 e1039.
- 1046 Bonev, B., and Cavalli, G. (2016). Organization and function of the 3D genome. *Nat Rev Genet*
1047 *17*, 661-678.
- 1048 Channappanavar, R., Fehr, A.R., Vijay, R., Mack, M., Zhao, J., Meyerholz, D.K., and Perlman,
1049 S. (2016). Dysregulated Type I Interferon and Inflammatory Monocyte-Macrophage Responses
1050 Cause Lethal Pneumonia in SARS-CoV-Infected Mice. *Cell Host Microbe* *19*, 181-193.
- 1051 Channappanavar, R., Fehr, A.R., Zheng, J., Wohlford-Lenane, C., Abrahante, J.E., Mack, M.,
1052 Sompallae, R., McCray, P.B., Jr., Meyerholz, D.K., and Perlman, S. (2019). IFN-I response
1053 timing relative to virus replication determines MERS coronavirus infection outcomes. *J Clin*
1054 *Invest* *129*, 3625-3639.
- 1055 Channappanavar, R., and Perlman, S. (2017). Pathogenic human coronavirus infections:
1056 causes and consequences of cytokine storm and immunopathology. *Semin Immunopathol* *39*,
1057 529-539.
- 1058 Chen, G., Wu, D., Guo, W., Cao, Y., Huang, D., Wang, H., Wang, T., Zhang, X., Chen, H., Yu,
1059 H., *et al.* (2020). Clinical and immunological features of severe and moderate coronavirus
1060 disease 2019. *J Clin Invest* *130*, 2620-2629.
- 1061 Chen, L.F., Lin, Y.T., Gallegos, D.A., Hazlett, M.F., Gomez-Schiavon, M., Yang, M.G., Kalmeta,
1062 B., Zhou, A.S., Holtzman, L., Gersbach, C.A., *et al.* (2019). Enhancer Histone Acetylation
1063 Modulates Transcriptional Bursting Dynamics of Neuronal Activity-Inducible Genes. *Cell Rep*
1064 *26*, 1174-1188 e1175.
- 1065 Cheung, C.Y., Poon, L.L., Ng, I.H., Luk, W., Sia, S.F., Wu, M.H., Chan, K.H., Yuen, K.Y.,
1066 Gordon, S., Guan, Y., *et al.* (2005). Cytokine responses in severe acute respiratory syndrome

- 1067 coronavirus-infected macrophages in vitro: possible relevance to pathogenesis. *J Virol* 79,
1068 7819-7826.
- 1069 Cummings, M.J., Baldwin, M.R., Abrams, D., Jacobson, S.D., Meyer, B.J., Balough, E.M.,
1070 Aaron, J.G., Claassen, J., Rabbani, L.E., Hastie, J., *et al.* (2020). Epidemiology, clinical course,
1071 and outcomes of critically ill adults with COVID-19 in New York City: a prospective cohort study.
1072 *Lancet* 395, 1763-1770.
- 1073 Daniloski, Z., Jordan, T.X., Wessels, H.H., Hoagland, D.A., Kasela, S., Legut, M., Maniatis, S.,
1074 Mimitou, E.P., Lu, L., Geller, E., *et al.* (2020). Identification of Required Host Factors for SARS-
1075 CoV-2 Infection in Human Cells. *Cell*.
- 1076 Del Valle, D.M., Kim-Schulze, S., Huang, H.H., Beckmann, N.D., Nirenberg, S., Wang, B.,
1077 Lavin, Y., Swartz, T.H., Madduri, D., Stock, A., *et al.* (2020). An inflammatory cytokine signature
1078 predicts COVID-19 severity and survival. *Nat Med* 26, 1636-1643.
- 1079 Dobin, A., Davis, C.A., Schlesinger, F., Drenkow, J., Zaleski, C., Jha, S., Batut, P., Chaisson,
1080 M., and Gingeras, T.R. (2013). STAR: ultrafast universal RNA-seq aligner. *Bioinformatics* 29,
1081 15-21.
- 1082 Fukaya, T., Lim, B., and Levine, M. (2016). Enhancer Control of Transcriptional Bursting. *Cell*
1083 166, 358-368.
- 1084 Garg, S., Kim, L., Whitaker, M., O'Halloran, A., Cummings, C., Holstein, R., Prill, M., Chai, S.J.,
1085 Kirley, P.D., Alden, N.B., *et al.* (2020). Hospitalization Rates and Characteristics of Patients
1086 Hospitalized with Laboratory-Confirmed Coronavirus Disease 2019 - COVID-NET, 14 States,
1087 March 1-30, 2020. *MMWR Morb Mortal Wkly Rep* 69, 458-464.
- 1088 Giamarellos-Bourboulis, E.J., Netea, M.G., Rovina, N., Akinosoglou, K., Antoniadou, A.,
1089 Antonakos, N., Damoraki, G., Gkavogianni, T., Adami, M.E., Katsaounou, P., *et al.* (2020).
1090 Complex Immune Dysregulation in COVID-19 Patients with Severe Respiratory Failure. *Cell*
1091 *Host Microbe* 27, 992-1000 e1003.
- 1092 Grajales-Reyes, G.E., and Colonna, M. (2020). Interferon responses in viral pneumonias.
1093 *Science* 369, 626-627.
- 1094 Group, W.H.O.R.E.A.f.C.-T.W., Sterne, J.A.C., Murthy, S., Diaz, J.V., Slutsky, A.S., Villar, J.,
1095 Angus, D.C., Annane, D., Azevedo, L.C.P., Berwanger, O., *et al.* (2020). Association Between
1096 Administration of Systemic Corticosteroids and Mortality Among Critically Ill Patients With
1097 COVID-19: A Meta-analysis. *JAMA* 324, 1330-1341.
- 1098 Guichard, S., Montazeri, A., Chatelut, E., Hennebelle, I., Bugat, R., and Canal, P. (2001).
1099 Schedule-dependent activity of topotecan in OVCAR-3 ovarian carcinoma xenograft:
1100 pharmacokinetic and pharmacodynamic evaluation. *Clin Cancer Res* 7, 3222-3228.
- 1101 Heinz, S., Benner, C., Spann, N., Bertolino, E., Lin, Y.C., Laslo, P., Cheng, J.X., Murre, C.,
1102 Singh, H., and Glass, C.K. (2010). Simple combinations of lineage-determining transcription
1103 factors prime cis-regulatory elements required for macrophage and B cell identities. *Mol Cell* 38,
1104 576-589.

- 1105 Heinz, S., Texari, L., Hayes, M.G.B., Urbanowski, M., Chang, M.W., Givarkes, N., Rialdi, A.,
1106 White, K.M., Albrecht, R.A., Pache, L., *et al.* (2018). Transcription Elongation Can Affect
1107 Genome 3D Structure. *Cell* *174*, 1522-1536 e1522.
- 1108 Hermine, O., Mariette, X., Tharaux, P.L., Resche-Rigon, M., Porcher, R., Ravaud, P., and
1109 Group, C.-C. (2020). Effect of Tocilizumab vs Usual Care in Adults Hospitalized With COVID-19
1110 and Moderate or Severe Pneumonia: A Randomized Clinical Trial. *JAMA Intern Med*.
- 1111 Hildebrand, E.M., and Dekker, J. (2020). Mechanisms and Functions of Chromosome
1112 Compartmentalization. *Trends Biochem Sci* *45*, 385-396.
- 1113 Hnisz, D., Day, D.S., and Young, R.A. (2016). Insulated Neighborhoods: Structural and
1114 Functional Units of Mammalian Gene Control. *Cell* *167*, 1188-1200.
- 1115 Houghton, P.J., Cheshire, P.J., Hallman, J.D., 2nd, Lutz, L., Friedman, H.S., Danks, M.K., and
1116 Houghton, J.A. (1995). Efficacy of topoisomerase I inhibitors, topotecan and irinotecan,
1117 administered at low dose levels in protracted schedules to mice bearing xenografts of human
1118 tumors. *Cancer Chemother Pharmacol* *36*, 393-403.
- 1119 Huang, C., Wang, Y., Li, X., Ren, L., Zhao, J., Hu, Y., Zhang, L., Fan, G., Xu, J., Gu, X., *et al.*
1120 (2020). Clinical features of patients infected with 2019 novel coronavirus in Wuhan, China.
1121 *Lancet* *395*, 497-506.
- 1122 Kollmannsberger, C., Mross, K., Jakob, A., Kanz, L., and Bokemeyer, C. (1999). Topotecan - A
1123 novel topoisomerase I inhibitor: pharmacology and clinical experience. *Oncology* *56*, 1-12.
- 1124 Korotkevich, G., Sukhov, V., and Sergushichev, A. (2019). Fast gene set enrichment analysis.
1125 bioRxiv, 060012.
- 1126 Lambert, S.A., Yang, A.W.H., Sasse, A., Cowley, G., Albu, M., Caddick, M.X., Morris, Q.D.,
1127 Weirauch, M.T., and Hughes, T.R. (2019). Similarity regression predicts evolution of
1128 transcription factor sequence specificity. *Nat Genet* *51*, 981-989.
- 1129 Langmead, B., and Salzberg, S.L. (2012). Fast gapped-read alignment with Bowtie 2. *Nat*
1130 *Methods* *9*, 357-359.
- 1131 Law, C.W., Chen, Y., Shi, W., and Smyth, G.K. (2014). voom: Precision weights unlock linear
1132 model analysis tools for RNA-seq read counts. *Genome Biol* *15*, R29.
- 1133 Lee, S., Channappanavar, R., and Kanneganti, T.D. (2020). Coronaviruses: Innate Immunity,
1134 Inflammasome Activation, Inflammatory Cell Death, and Cytokines. *Trends Immunol*.
- 1135 Lei, X., Dong, X., Ma, R., Wang, W., Xiao, X., Tian, Z., Wang, C., Wang, Y., Li, L., Ren, L., *et al.*
1136 (2020). Activation and evasion of type I interferon responses by SARS-CoV-2. *Nat Commun* *11*,
1137 3810.
- 1138 Li, H., Handsaker, B., Wysoker, A., Fennell, T., Ruan, J., Homer, N., Marth, G., Abecasis, G.,
1139 Durbin, R., and Genome Project Data Processing, S. (2009). The Sequence Alignment/Map
1140 format and SAMtools. *Bioinformatics* *25*, 2078-2079.

- 1141 Liao, Y., Smyth, G.K., and Shi, W. (2014). featureCounts: an efficient general purpose program
1142 for assigning sequence reads to genomic features. *Bioinformatics* 30, 923-930.
- 1143 Lin, Y.C., Benner, C., Mansson, R., Heinz, S., Miyazaki, K., Miyazaki, M., Chandra, V., Bossen,
1144 C., Glass, C.K., and Murre, C. (2012). Global changes in the nuclear positioning of genes and
1145 intra- and interdomain genomic interactions that orchestrate B cell fate. *Nat Immunol* 13, 1196-
1146 1204.
- 1147 Liu, X., Hong, T., Parameswaran, S., Ernst, K., Marazzi, I., Weirauch, M.T., and Fuxman Bass,
1148 J.I. (2020). Human Virus Transcriptional Regulators. *Cell* 182, 24-37.
- 1149 Livingston, E., and Bucher, K. (2020). Coronavirus Disease 2019 (COVID-19) in Italy. *JAMA*
1150 323, 1335.
- 1151 Love, M.I., Huber, W., and Anders, S. (2014). Moderated estimation of fold change and
1152 dispersion for RNA-seq data with DESeq2. *Genome Biol* 15, 550.
- 1153 Lucas, C., Wong, P., Klein, J., Castro, T.B.R., Silva, J., Sundaram, M., Ellingson, M.K., Mao, T.,
1154 Oh, J.E., Israelow, B., *et al.* (2020). Longitudinal analyses reveal immunological misfiring in
1155 severe COVID-19. *Nature* 584, 463-469.
- 1156 Marazzi, I., Greenbaum, B.D., Low, D.H.P., and Guccione, E. (2018). Chromatin dependencies
1157 in cancer and inflammation. *Nat Rev Mol Cell Biol* 19, 245-261.
- 1158 Marazzi, I., Ho, J.S., Kim, J., Manicassamy, B., Dewell, S., Albrecht, R.A., Seibert, C.W.,
1159 Schaefer, U., Jeffrey, K.L., Prinjha, R.K., *et al.* (2012). Suppression of the antiviral response by
1160 an influenza histone mimic. *Nature* 483, 428-433.
- 1161 Martin, M. (2011). Cutadapt removes adapter sequences from high-throughput sequencing
1162 reads. *2011* 17, 3.
- 1163 Mathijssen, R.H., van Alphen, R.J., Verweij, J., Loos, W.J., Nooter, K., Stoter, G., and
1164 Sparreboom, A. (2001). Clinical pharmacokinetics and metabolism of irinotecan (CPT-11). *Clin*
1165 *Cancer Res* 7, 2182-2194.
- 1166 Merad, M., and Martin, J.C. (2020). Pathological inflammation in patients with COVID-19: a key
1167 role for monocytes and macrophages. *Nat Rev Immunol* 20, 355-362.
- 1168 Miller, M.S., Rialdi, A., Ho, J.S., Tilove, M., Martinez-Gil, L., Moshkina, N.P., Peralta, Z., Noel,
1169 J., Melegari, C., Maestre, A.M., *et al.* (2015). Senataxin suppresses the antiviral transcriptional
1170 response and controls viral biogenesis. *Nat Immunol* 16, 485-494.
- 1171 Moore, J.B., and June, C.H. (2020). Cytokine release syndrome in severe COVID-19. *Science*
1172 368, 473-474.
- 1173 Munoz-Fontela, C., Dowling, W.E., Funnell, S.G.P., Gsell, P.S., Riveros-Balta, A.X., Albrecht,
1174 R.A., Andersen, H., Baric, R.S., Carroll, M.W., Cavaleri, M., *et al.* (2020). Animal models for
1175 COVID-19. *Nature* 586, 509-515.
- 1176 Nemati, F., Daniel, C., Arvelo, F., Legrier, M.E., Froget, B., Livartowski, A., Assayag, F.,
1177 Bourgeois, Y., Poupon, M.F., and Decaudin, D. (2010). Clinical relevance of human cancer

- 1178 xenografts as a tool for preclinical assessment: example of in-vivo evaluation of topotecan-
1179 based chemotherapy in a panel of human small-cell lung cancer xenografts. *Anticancer Drugs*
1180 *21*, 25-32.
- 1181 Nicodeme, E., Jeffrey, K.L., Schaefer, U., Beinke, S., Dewell, S., Chung, C.W., Chandwani, R.,
1182 Marazzi, I., Wilson, P., Coste, H., *et al.* (2010). Suppression of inflammation by a synthetic
1183 histone mimic. *Nature* *468*, 1119-1123.
- 1184 Nienhold, R., Ciani, Y., Koelzer, V.H., Tzankov, A., Haslbauer, J.D., Menter, T., Schwab, N.,
1185 Henkel, M., Frank, A., Zsikla, V., *et al.* (2020). Two distinct immunopathological profiles in
1186 autopsy lungs of COVID-19. *Nat Commun* *11*, 5086.
- 1187 O'Driscoll, M., Dos Santos, G.R., Wang, L., Cummings, D.A.T., Azman, A.S., Paireau, J.,
1188 Fontanet, A., Cauchemez, S., and Salje, H. (2020). Age-specific mortality and immunity patterns
1189 of SARS-CoV-2. *Nature*.
- 1190 Oran, D.P., and Topol, E.J. (2020). Prevalence of Asymptomatic SARS-CoV-2 Infection : A
1191 Narrative Review. *Ann Intern Med* *173*, 362-367.
- 1192 Pedregosa, F., Varoquaux, G., Gramfort, A., Michel, V., Thirion, B., Grisel, O., Blondel, M.,
1193 Prettenhofer, P., Weiss, R., Dubourg, V., *et al.* (2011). Scikit-learn: Machine Learning in Python.
1194 *Journal of Machine Learning Research* *12*, 2825-2830.
- 1195 Qin, C., Zhou, L., Hu, Z., Zhang, S., Yang, S., Tao, Y., Xie, C., Ma, K., Shang, K., Wang, W., *et*
1196 *al.* (2020). Dysregulation of Immune Response in Patients With Coronavirus 2019 (COVID-19)
1197 in Wuhan, China. *Clin Infect Dis* *71*, 762-768.
- 1198 Quinlan, A.R., and Hall, I.M. (2010). BEDTools: a flexible suite of utilities for comparing genomic
1199 features. *Bioinformatics* *26*, 841-842.
- 1200 Rao, S.S.P., Huang, S.C., Glenn St Hilaire, B., Engreitz, J.M., Perez, E.M., Kieffer-Kwon, K.R.,
1201 Sanborn, A.L., Johnstone, S.E., Bascom, G.D., Bochkov, I.D., *et al.* (2017). Cohesin Loss
1202 Eliminates All Loop Domains. *Cell* *171*, 305-320 e324.
- 1203 Rialdi, A., Campisi, L., Zhao, N., Lagda, A.C., Pietzsch, C., Ho, J.S.Y., Martinez-Gil, L., Fenouil,
1204 R., Chen, X., Edwards, M., *et al.* (2016). Topoisomerase 1 inhibition suppresses inflammatory
1205 genes and protects from death by inflammation. *Science* *352*, aad7993.
- 1206 Ritchie, M.E., Phipson, B., Wu, D., Hu, Y., Law, C.W., Shi, W., and Smyth, G.K. (2015). limma
1207 powers differential expression analyses for RNA-sequencing and microarray studies. *Nucleic*
1208 *Acids Res* *43*, e47.
- 1209 Rowinsky, E.K., Grochow, L.B., Hendricks, C.B., Ettinger, D.S., Forastiere, A.A., Hurowitz, L.A.,
1210 McGuire, W.P., Sartorius, S.E., Lubejko, B.G., Kaufmann, S.H., *et al.* (1992). Phase I and
1211 pharmacologic study of topotecan: a novel topoisomerase I inhibitor. *J Clin Oncol* *10*, 647-656.
- 1212 Salvarani, C., Dolci, G., Massari, M., Merlo, D.F., Cavuto, S., Savoldi, L., Bruzzi, P., Boni, F.,
1213 Braglia, L., Turra, C., *et al.* (2020). Effect of Tocilizumab vs Standard Care on Clinical
1214 Worsening in Patients Hospitalized With COVID-19 Pneumonia: A Randomized Clinical Trial.
1215 *JAMA Intern Med*.

- 1216 Schwarzer, W., Abdennur, N., Goloborodko, A., Pekowska, A., Fudenberg, G., Loe-Mie, Y.,
1217 Fonseca, N.A., Huber, W., Haering, C.H., Mirny, L., *et al.* (2017). Two independent modes of
1218 chromatin organization revealed by cohesin removal. *Nature* 551, 51-56.
- 1219 Senecal, A., Munsky, B., Proux, F., Ly, N., Braye, F.E., Zimmer, C., Mueller, F., and Darzacq, X.
1220 (2014). Transcription factors modulate c-Fos transcriptional bursts. *Cell Rep* 8, 75-83.
- 1221 Siddiqi, H.K., and Mehra, M.R. (2020). COVID-19 illness in native and immunosuppressed
1222 states: A clinical-therapeutic staging proposal. *J Heart Lung Transplant* 39, 405-407.
- 1223 Slutsky, A.S., and Ranieri, V.M. (2013). Ventilator-induced lung injury. *N Engl J Med* 369, 2126-
1224 2136.
- 1225 Stokes, E.K., Zambrano, L.D., Anderson, K.N., Marder, E.P., Raz, K.M., El Burai Felix, S., Tie,
1226 Y., and Fullerton, K.E. (2020). Coronavirus Disease 2019 Case Surveillance - United States,
1227 January 22-May 30, 2020. *MMWR Morb Mortal Wkly Rep* 69, 759-765.
- 1228 Subramanian, A., Tamayo, P., Mootha, V.K., Mukherjee, S., Ebert, B.L., Gillette, M.A.,
1229 Paulovich, A., Pomeroy, S.L., Golub, T.R., Lander, E.S., *et al.* (2005). Gene set enrichment
1230 analysis: a knowledge-based approach for interpreting genome-wide expression profiles. *Proc*
1231 *Natl Acad Sci U S A* 102, 15545-15550.
- 1232 Tang, Y., Liu, J., Zhang, D., Xu, Z., Ji, J., and Wen, C. (2020). Cytokine Storm in COVID-19:
1233 The Current Evidence and Treatment Strategies. *Front Immunol* 11, 1708.
- 1234 von Pawel, J., Schiller, J.H., Shepherd, F.A., Fields, S.Z., Kleisbauer, J.P., Chrysson, N.G.,
1235 Stewart, D.J., Clark, P.I., Palmer, M.C., Depierre, A., *et al.* (1999). Topotecan versus
1236 cyclophosphamide, doxorubicin, and vincristine for the treatment of recurrent small-cell lung
1237 cancer. *J Clin Oncol* 17, 658-667.
- 1238 Wang, D., Hu, B., Hu, C., Zhu, F., Liu, X., Zhang, J., Wang, B., Xiang, H., Cheng, Z., Xiong, Y.,
1239 *et al.* (2020a). Clinical Characteristics of 138 Hospitalized Patients With 2019 Novel
1240 Coronavirus-Infected Pneumonia in Wuhan, China. *JAMA* 323, 1061-1069.
- 1241 Wang, D., Li, R., Wang, J., Jiang, Q., Gao, C., Yang, J., Ge, L., and Hu, Q. (2020b). Correlation
1242 analysis between disease severity and clinical and biochemical characteristics of 143 cases of
1243 COVID-19 in Wuhan, China: a descriptive study. *BMC Infect Dis* 20, 519.
- 1244 Winkler, E.S., Bailey, A.L., Kafai, N.M., Nair, S., McCune, B.T., Yu, J., Fox, J.M., Chen, R.E.,
1245 Earnest, J.T., Keeler, S.P., *et al.* (2020). SARS-CoV-2 infection of human ACE2-transgenic
1246 mice causes severe lung inflammation and impaired function. *Nat Immunol* 21, 1327-1335.
- 1247 Wong, C.K., Lam, C.W., Wu, A.K., Ip, W.K., Lee, N.L., Chan, I.H., Lit, L.C., Hui, D.S., Chan,
1248 M.H., Chung, S.S., *et al.* (2004). Plasma inflammatory cytokines and chemokines in severe
1249 acute respiratory syndrome. *Clin Exp Immunol* 136, 95-103.
- 1250 Wu, C., Chen, X., Cai, Y., Xia, J., Zhou, X., Xu, S., Huang, H., Zhang, L., Zhou, X., Du, C., *et al.*
1251 (2020). Risk Factors Associated With Acute Respiratory Distress Syndrome and Death in
1252 Patients With Coronavirus Disease 2019 Pneumonia in Wuhan, China. *JAMA Intern Med* 180,
1253 934-943.

- 1254 Wu, Z., and McGoogan, J.M. (2020). Characteristics of and Important Lessons From the
1255 Coronavirus Disease 2019 (COVID-19) Outbreak in China: Summary of a Report of 72314
1256 Cases From the Chinese Center for Disease Control and Prevention. *JAMA* *323*, 1239-1242.
- 1257 Yang, X., Yu, Y., Xu, J., Shu, H., Xia, J., Liu, H., Wu, Y., Zhang, L., Yu, Z., Fang, M., *et al.*
1258 (2020a). Clinical course and outcomes of critically ill patients with SARS-CoV-2 pneumonia in
1259 Wuhan, China: a single-centered, retrospective, observational study. *Lancet Respir Med* *8*, 475-
1260 481.
- 1261 Yang, Y., Shen, C., Li, J., Yuan, J., Wei, J., Huang, F., Wang, F., Li, G., Li, Y., Xing, L., *et al.*
1262 (2020b). Plasma IP-10 and MCP-3 levels are highly associated with disease severity and
1263 predict the progression of COVID-19. *J Allergy Clin Immunol* *146*, 119-127 e114.
- 1264 Zabidi, M.A., Arnold, C.D., Schernhuber, K., Pagani, M., Rath, M., Frank, O., and Stark, A.
1265 (2015). Enhancer-core-promoter specificity separates developmental and housekeeping gene
1266 regulation. *Nature* *518*, 556-559.
- 1267 Zhang, Y., Liu, T., Meyer, C.A., Eeckhoutte, J., Johnson, D.S., Bernstein, B.E., Nusbaum, C.,
1268 Myers, R.M., Brown, M., Li, W., *et al.* (2008). Model-based analysis of ChIP-Seq (MACS).
1269 *Genome Biol* *9*, R137.
- 1270 Zhou, F., Yu, T., Du, R., Fan, G., Liu, Y., Liu, Z., Xiang, J., Wang, Y., Song, B., Gu, X., *et al.*
1271 (2020a). Clinical course and risk factors for mortality of adult inpatients with COVID-19 in
1272 Wuhan, China: a retrospective cohort study. *Lancet* *395*, 1054-1062.
- 1273 Zhou, Y., Fu, B., Zheng, X., Wang, D., Zhao, C., Qi, Y., Sun, R., Tian, Z., Xu, X., and Wei, H.
1274 (2020b). Pathogenic T-cells and inflammatory monocytes incite inflammatory storms in severe
1275 COVID-19 patients. *National Science Review* *7*, 998-1002.
- 1276 Zhu, Z., Lian, X., Su, X., Wu, W., Marraro, G.A., and Zeng, Y. (2020). From SARS and MERS to
1277 COVID-19: a brief summary and comparison of severe acute respiratory infections caused by
1278 three highly pathogenic human coronaviruses. *Respir Res* *21*, 224.
- 1279
1280

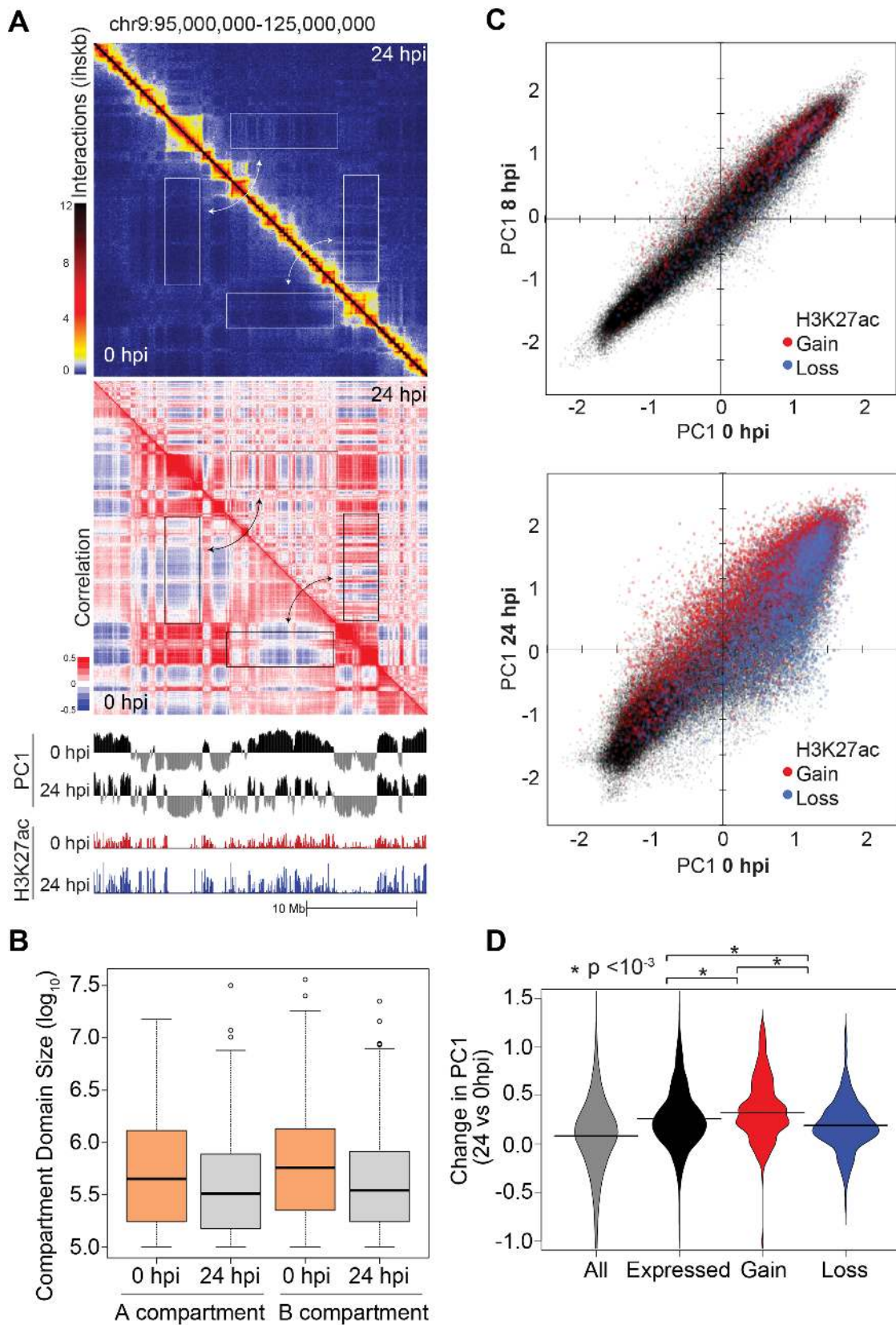
FIGURE 1

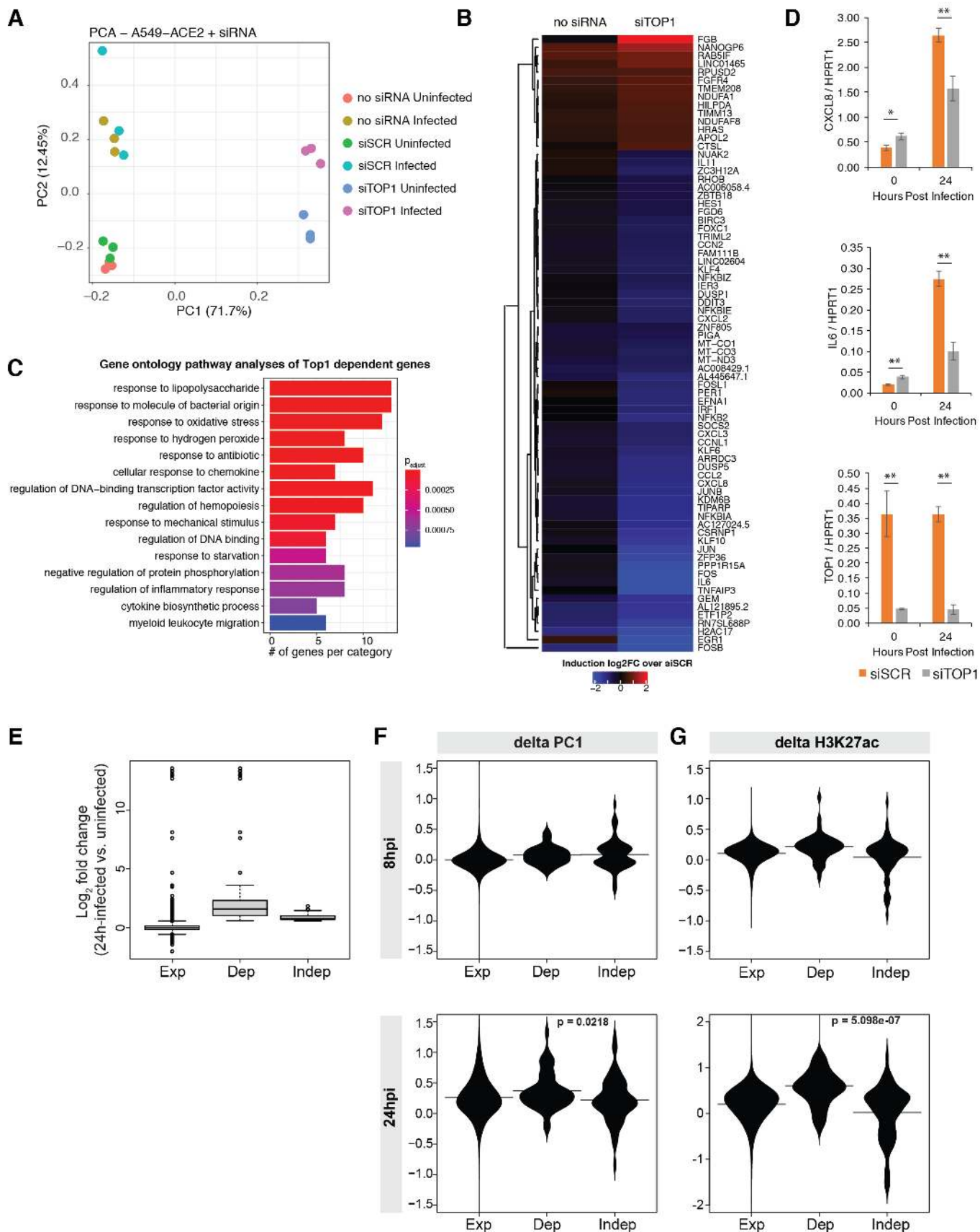
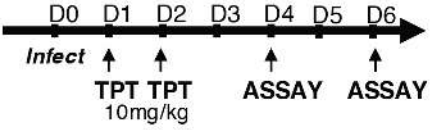
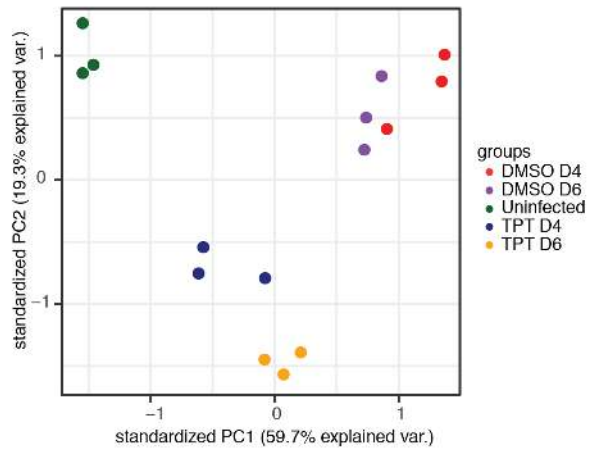
FIGURE 2

FIGURE 3

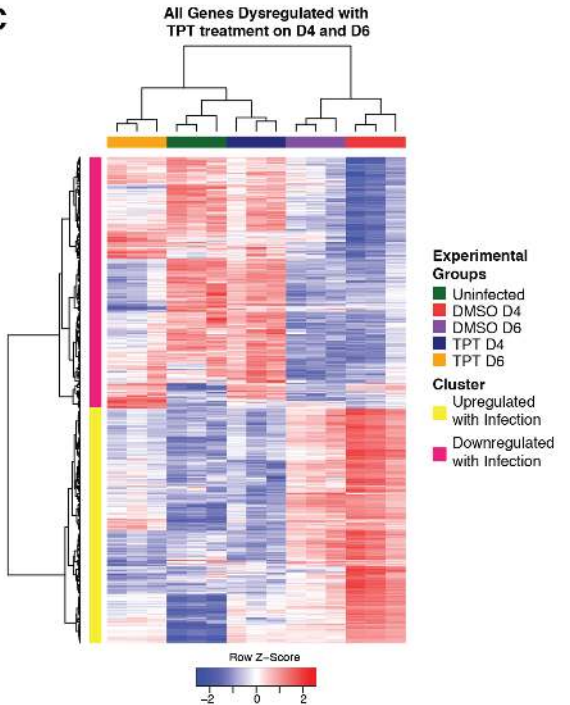
A



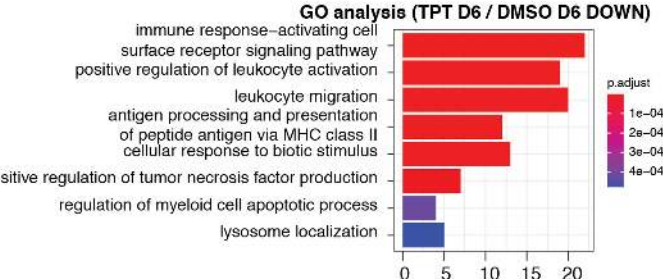
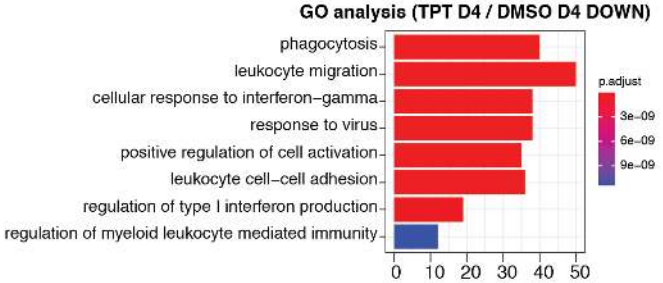
B



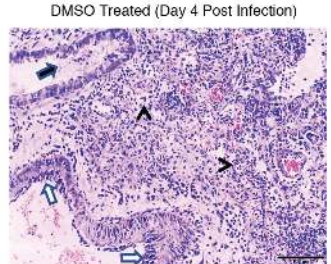
C



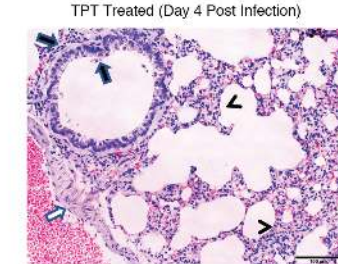
D



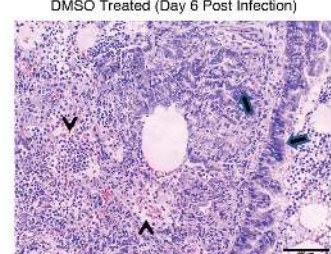
E



G



F

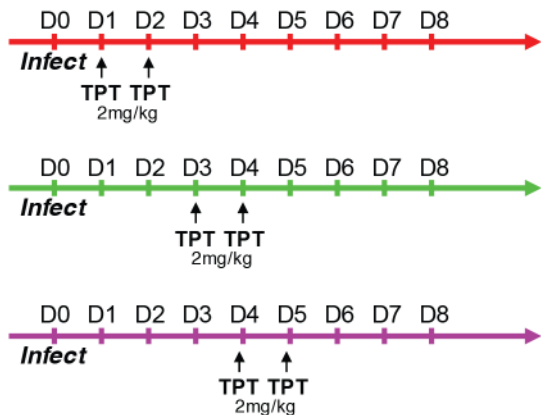


H

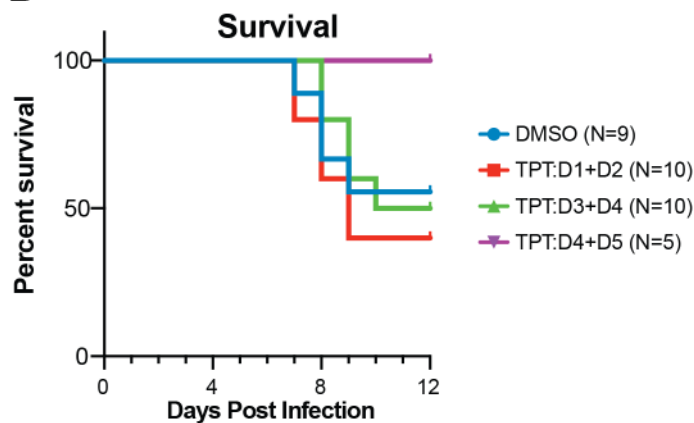


FIGURE 5

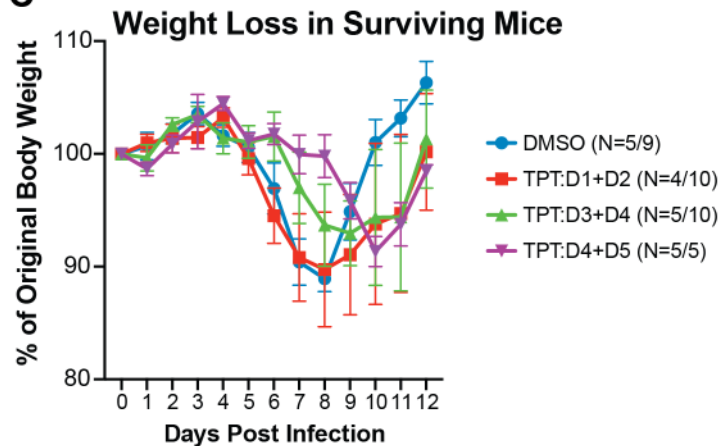
A



B



C



D

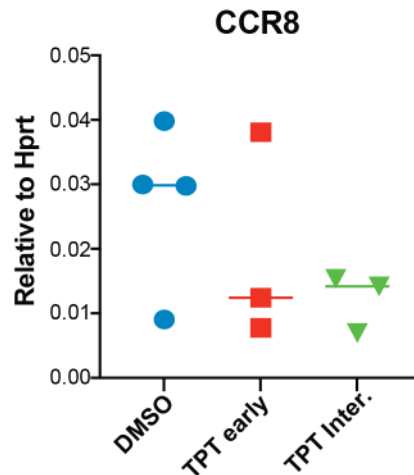
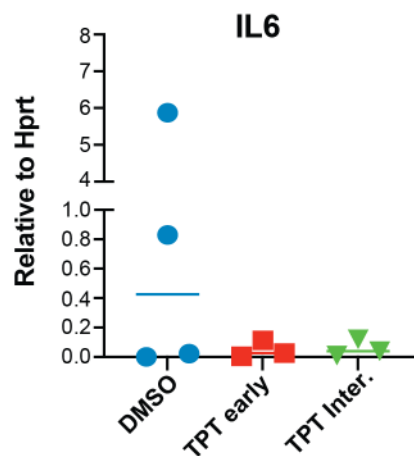
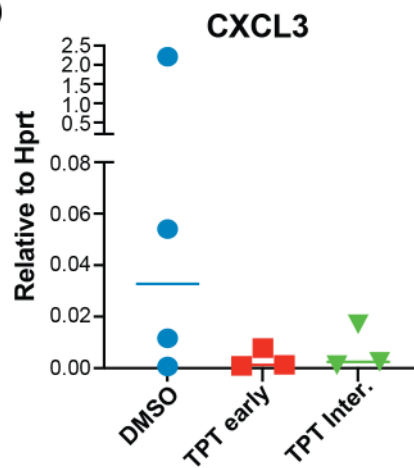
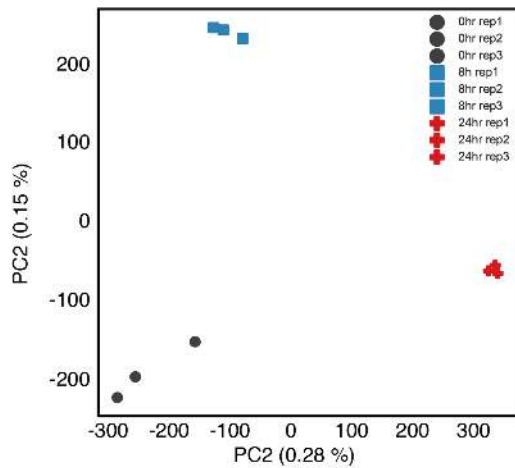
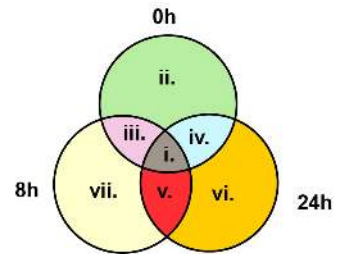


FIGURE S1

A

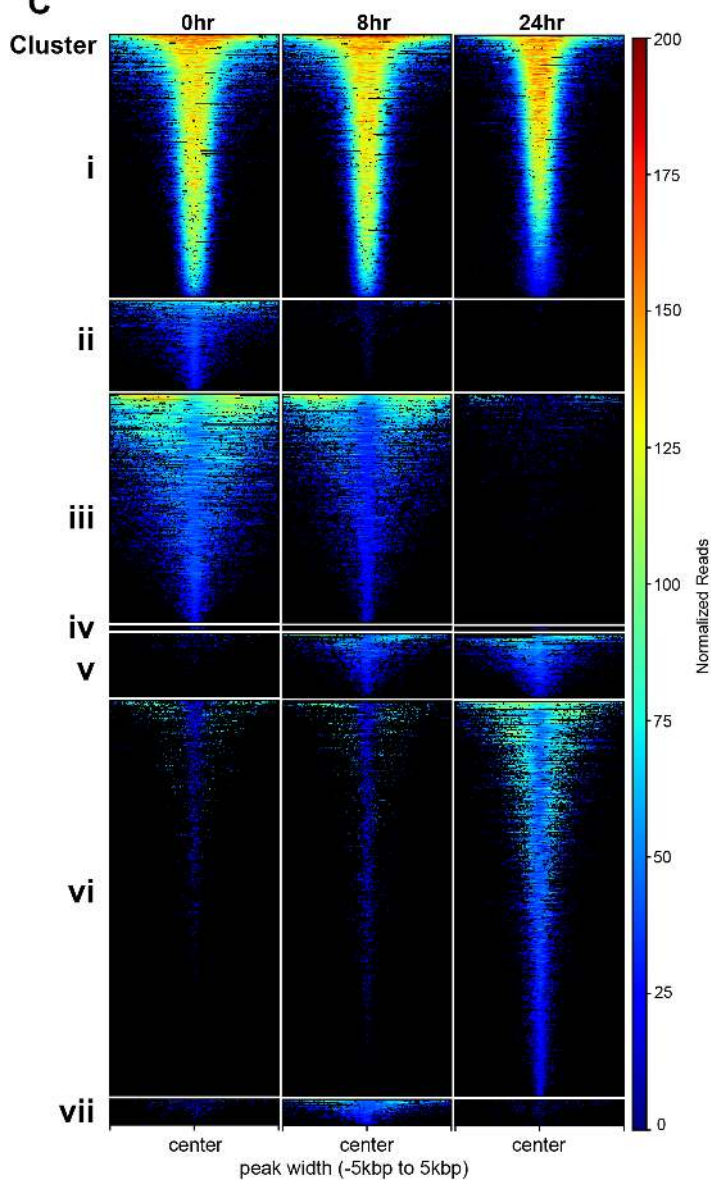


B



Cluster	0h/8h/24h	Number of peaks
i.	ON-ON-ON	8995
ii.	ON-OFF-OFF	3073
iii.	ON-ON-OFF	7837
iv.	ON-OFF-ON	126
v.	OFF-ON-ON	2169
vi.	OFF-OFF-ON	13546
vii.	OFF-ON-OFF	879

C



D

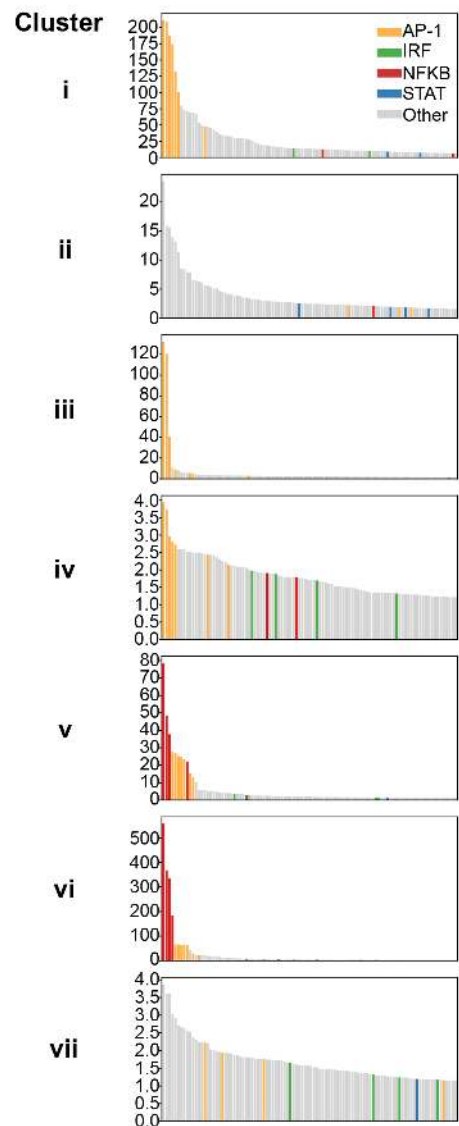
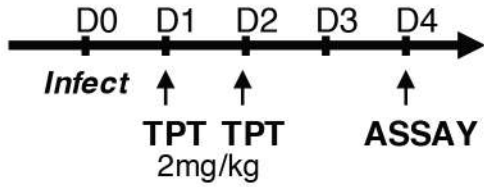
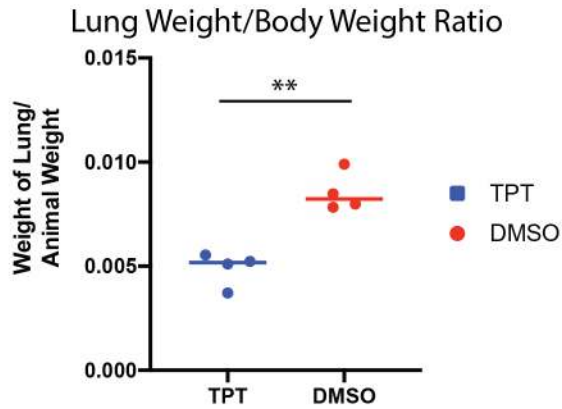


FIGURE S2

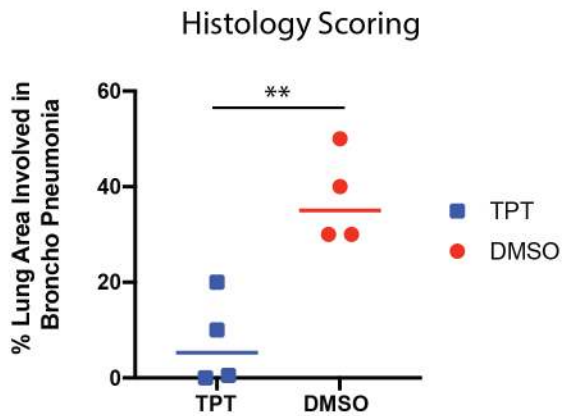
A



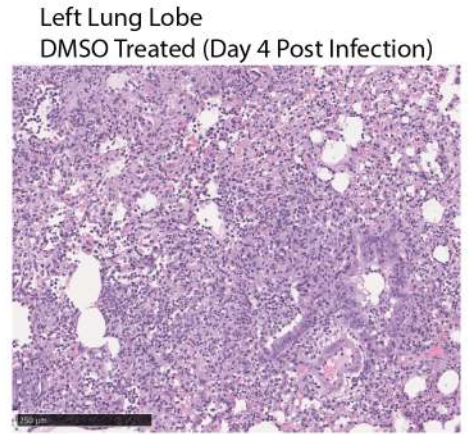
B



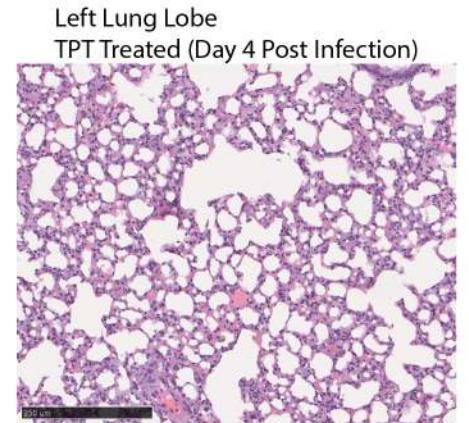
C



D



E



F

